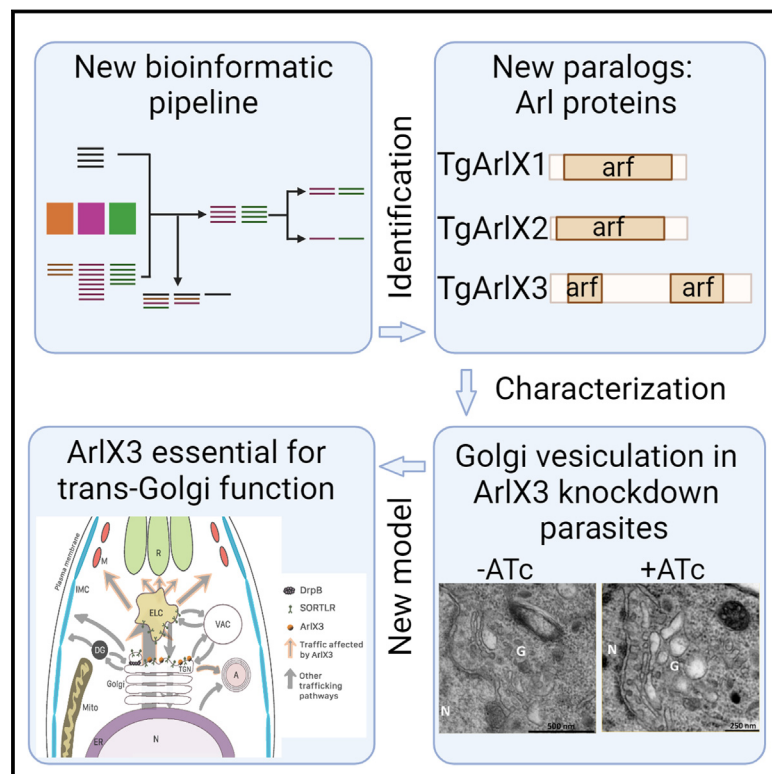# Evolutionary analysis identifies a Golgi pathway and correlates lineage-specific factors with endomembrane organelle emergence in apicomplexans

Graphical abstract

Authors

Christen M. Klinger, Elena Jimenez-Ruiz, Tobias Mourier, ..., Arnab Pain, Joel B. Dacks, Markus Meissner

Correspondence

dacks@ualberta.ca (J.B.D.), markus.meissner@lmu.de (M.M.)

In brief

Unique membrane-trafficking pathways or organelles are proposed to coincide with the expansion and specialization of trafficking factors. Using the parasite *Toxoplasma gondii* as a model system, Klinger et al. identified the myzozoan-specific trafficking factor ArlX3 as critical for post-Golgi transport to unique secretory organelles, micronemes, and rhoptries.

Highlights

- Many lineage-specific membrane-trafficking paralogs exist in the apicomplexans

- Myzozoan-specific ArlX3 mediates post-Golgi transport to micronemes and rhoptries

- Emergence of paralogs coincides with new organelles or pathways in this lineage

CellPress

Report

Evolutionary analysis identifies a Golgi pathway and correlates lineage-specific factors with endomembrane organelle emergence in apicomplexans

Christen M. Klinger,[1,2,10] Elena Jimenez-Ruiz,[3,10] Tobias Mourier,[4] Andreas Klingl,[5] Leandro Lemgruber,[6] Arnab Pain,[4,7] Joel B. Dacks,[1,2,8,9,*] and Markus Meissner[3,11,*]

[1]Division of Infectious Diseases, Department of Medicine and Department of Biological Sciences, University of Alberta, Edmonton, AB, Canada
[2]Women and Children's Health Research Institute, University of Alberta, Edmonton, AB, Canada
[3]Experimental Parasitology, Department of Veterinary Sciences, Faculty of Veterinary Medicine, Ludwig-Maximilians-Universität, LMU, Munich, Germany
[4]Pathogen Genomics Laboratory, Bioscience Programme, Biological, and Environmental Sciences and Engineering (BESE) Division, King Abdullah University of Science and Technology (KAUST), Thuwal 23955-6900, Kingdom of Saudi Arabia
[5]Pflanzliche Entwicklungsbiologie, Biozentrum der Ludwig-Maximilians-Universität, Munich, Germany
[6]Cellular Analysis Facility, College of Medical, Veterinary & Life Sciences, University of Glasgow, Glasgow, UK
[7]International Institute for Zoonosis Control, GI-CoRE, Hokkaido University, Sapporo, Japan
[8]Institute of Parasitology, Biology Centre, Czech Academy of Sciences, České Budějovice (Budweis), Czech Republic
[9]Centre for Life's Origin and Evolution, Department of Genetics, Evolution & Environment, University College London, London, UK
[10]These authors contributed equally
[11]Lead contact
*Correspondence: dacks@ualberta.ca (J.B.D.), markus.meissner@lmu.de (M.M.)
https://doi.org/10.1016/j.celrep.2024.113740

SUMMARY

The organelle paralogy hypothesis (OPH) aims to explain the evolution of non-endosymbiotically derived organelles. It predicts that lineage-specific pathways or organelles should result when identity-encoding membrane-trafficking components duplicate and co-evolve. Here, we investigate the presence of such lineage-specific membrane-trafficking machinery paralogs in Apicomplexa, a globally important parasitic lineage. We are able to identify 18 paralogs of known membrane-trafficking machinery, in several cases co-incident with the presence of new endomembrane organelles in apicomplexans or their parent lineage, the Alveolata. Moreover, focused analysis of the apicomplexan Arf-like small GTPases (i.e., ArlX3) revealed a specific post-Golgi trafficking pathway. This pathway appears involved in delivery of proteins to micronemes and rhoptries, with knockdown demonstrating reduced invasion capacity. Overall, our data have identified an unforeseen post-Golgi trafficking pathway in apicomplexans and are consistent with the OPH mechanism acting to produce endomembrane pathways or organelles at various evolutionary stages across the alveolate lineage.

INTRODUCTION

Eukaryotes are defined in part by the extensive presence of intracellular membrane-bound organelles. In addition to being a key stepping stone in eukaryotic evolution, the advent and expansion of organelles necessitated the development of protein machinery to facilitate the movement of protein and lipid components between organelles. The organelles and the machinery that mediates this movement together comprise the membrane-trafficking system (MTS), which is a key feature of all eukaryotes.[1]

The MTS machinery is responsible for cargo loading and vesicle formation, vesicle scission, vesicle transport from donor to acceptor compartment, and eventual vesicle tethering and fusion.[1,2] Notably, a large proportion of MTS machinery comprises paralogous gene families, wherein distinct paralogs

perform the same basic function at distinct cellular locations. This observation led to the proposal of the organelle paralogy hypothesis (OPH), which posits that the duplication and co-evolution of MTS machinery encoding organelle identity facilitated the diversification of an ancestral organelle(s) to give rise to the diversity of organelles found in modern eukaryotes.[3,4]

Molecular evolutionary studies have reconstructed the presence of an extensive MTS machinery complement in the last eukaryotic common ancestor (LECA).[5–9] Cell biological studies have confirmed a general conservation of organelles themselves, with most eukaryotes possessing identifiable homologs of an endoplasmic reticulum (ER), Golgi apparatus, early and late endolysosomal compartments, and peroxisomes.[1] Despite proteins with clear, deep homology for some of these MTS components in Archaea,[3,10,11] orthologs of the organelle or pathway-specific protein machinery are absent. The overall conclusion of
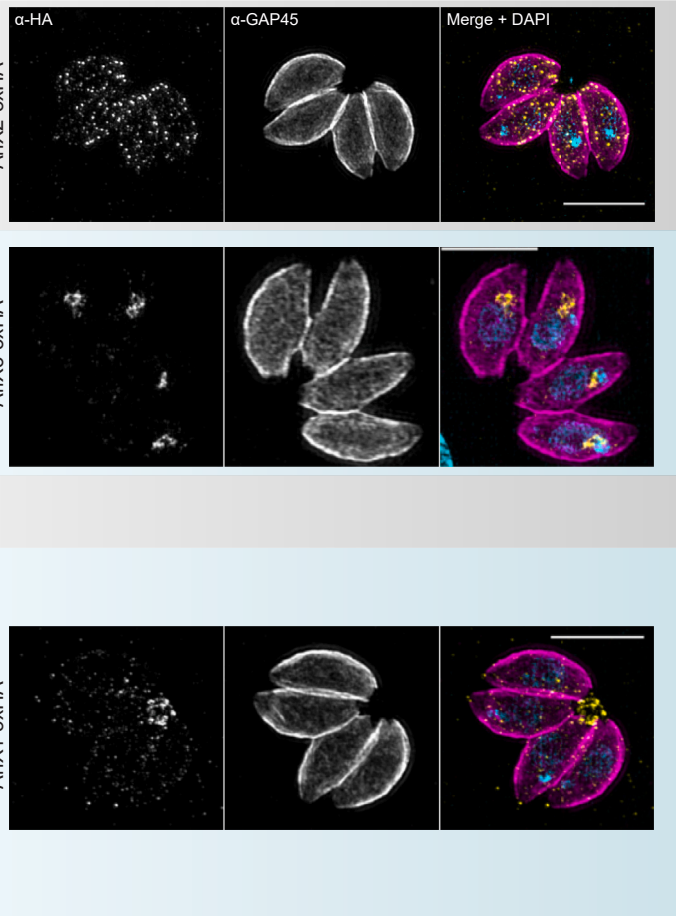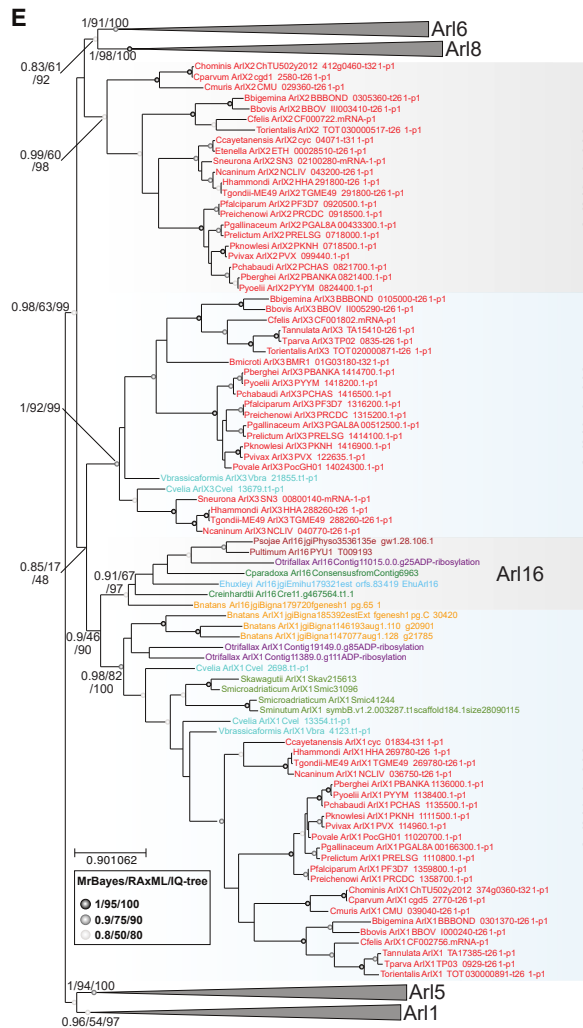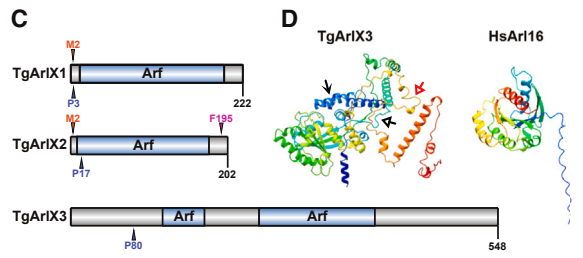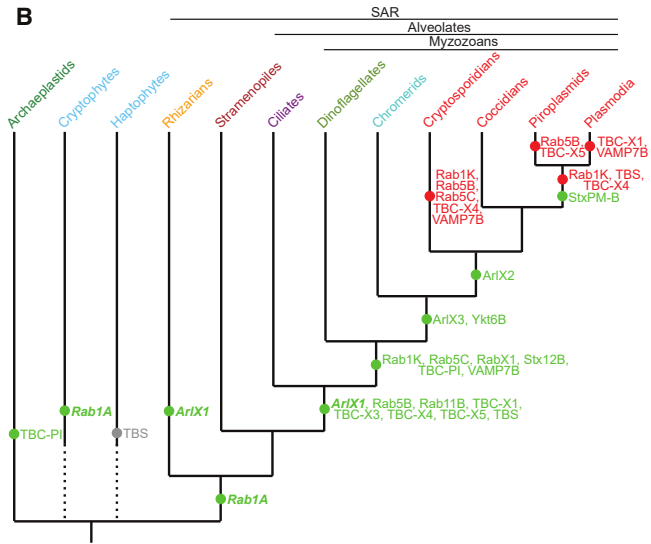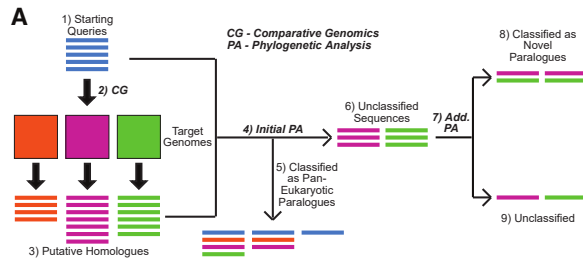
these data that ancestral MTS machinery present in the first eukaryotic common ancestor (FECA) expanded and diversified into a complex set of machinery in the LECA, complete with an extensive organelle complement.[3,4,12]

While the OPH was initially proposed to provide a mechanistic framework to explain the FECA-LECA MTS transition, we have previously argued that it is also likely to have continued functioning in eukaryotes post-LECA.[1,12] This argument is in part motivated by the presence of additional organelles in many eukaryotes, including secretory granules and melanosomes in human cells, as well as other enigmatic organelles such as the contractile vacuole and extrusomes present in diverse eukaryotes.[13,14] However, the extent and ways in which the OPH has shaped the diversity of lineage-specific endomembrane organelles are largely unexplored. Such an exploration requires a eukaryotic lineage with clear novel organelles, available genomic data, and, ideally, the capacity for molecular cell biological study.

The Apicomplexa is a phylum of unicellular eukaryotic parasites that invade the cells of a variety of hosts, including humans. Although almost universally parasitic, apicomplexans possess free-living relatives including chromerid (representing colpedellids) and dinoflagellate algae, many members of which are photo- or mixotrophic[15–17]; together, these taxa form a group known as the Myzozoa. Molecular and ultrastructural data support the presence of numerous novel hallmark organelles in apicomplexans, including the inner membrane complex (IMC, a series of connected membranous sacs subtending the plasma membrane),[18] a relict non-photosynthetic plastid (the apicoplast), dense granules, and the specialized endo-lysosomal-derived organelles micronemes and rhoptries. Notably, some of the above-mentioned apicomplexan organelles have presumed homologs in closely related taxa. Structures resembling micronemes and rhoptries are present in other myzozoans,[19] and the IMC is considered homologous to the alveoli of ciliates (which as a basal group to the Myzozoa form the alveolate clade).[20,21] In addition to the clear presence of distinctive organelles in apicomplexans and their close relatives, genomic data exist for all the main groups of alveolates, allowing for comparative genomic analyses. Within the Apicomplexa, *Toxoplasma gondii* provides

a useful system for conducting molecular biology due to its ease of culture, haploid genome, and available range of genetic tools.[22,23]

Hence, we set out to analyze the extent to which an OPH-like mechanism may have given rise to the novel organelles present in the Apicomplexa and their close relatives. Through large-scale comparative genomic and phylogenetic analyses, we were able to identify 18 paralogs of membrane-trafficking protein families found in Apicomplexa but not found across eukaryotes. Of these paralogs, we chose three, all from the ARF-related (Arl) family, for further investigation. Although we localize all three novel Arls in asexual *T. gondii* parasites, only one proved essential following genetic disruption. This protein, termed ArlX3, localizes primarily to the *trans*-Golgi network (TGN) and results in the mislocalization of microneme and rhoptry proteins when knocked down, as well as a general fragmentation of the Golgi itself. Overall, our results identify the presence of novel trafficking paralogs in a medically important and cell biologically distinctive group of eukaryotic parasites and provide insight into modern examples of the OPH shaping eukaryotic evolution.

RESULTS

A bioinformatics screen to identify lineage-specific paralogs in Apicomplexa and related taxa

To identify paralogs with a restricted phylogenetic distribution, hereafter referred to as lineage-specific paralogs (LSPs), we first carried out both HMMer and BLAST searches to identify all homologs for each family in our dataset (Data S2). Next, we carried out phylogenetic analyses using proteins of known identity to classify any pan-eukaryotic paralogs from a series of smaller taxon-specific datasets. Finally, we collected all previously unclassified sequences for each family and performed additional phylogenetic analyses to identify those that formed supported monophyletic clades; these clades were then run with previously classified pan-eukaryotic clades to establish their possible origins (Figure 1A, STAR Methods, Data S1).

We analyzed the following paralogous families for the presence of LSPs: SM proteins, SNARE proteins, Rab GTPases, the TBC family of Rab GTPase-activating proteins (RabGAPs),

---

Figure 1. A phylogenetic screen identifies LSPs in Apicomplexa and their close relatives

This figure summarizes the methodology behind, and results of, a phylogenetic screen to identify lineage-specific paralogs (LSPs) in apicomplexans.

(A) Overview of the screen. Homologs of each trafficking family were identified (1–3), and all pan-eukaryotic orthologs were identified via phylogenetic analysis with known marker sequences (4–5). Any unclassified sequences (6) were then run in additional phylogenetic analyses (7); some formed monophyletic clades (LSPs; 8), while others remained unclassified (9). CG: comparative genomics; PA: phylogenetic analysis.

(B) Summary of presumed patterns of gain (green text) and loss (red text) of LSPs in study taxa. Green dots represent gain, while red dots represent loss; bold italics represent uncertain provenance (between independent gain or ancient gain and subsequent loss). The single gray dot represents the presence of an analogous TBS protein in *E. huxleyi*. Taxa are color-coded: apicomplexan, red; chromerids, teal; dinoflagellates, light green; ciliates, purple; stramenopiles, brown; rhizarians, orange; cryptophytes/haptophytes, blue; archaeplastids, dark green. Larger taxonomic groups are summarized above.

(C) Schematic overview of Arl LSPs in *T. gondii*. Each sequence is represented as a gray bar (length shown below each), with Pfam Arf (Pfam: PF00025) domains in light blue. The highest-scoring predicted site for each type of lipid modification (F, farnesylation; M, myristoylation; P, palmitoylation) is shown.

(D) The AlphaFold 3D structure of TgArlX3 is shown, colored from N (red) to C terminus (blue). Arrows indicate the additional N-terminal helices (black arrow), an internal loop between the canonical Arf folds (black hollow arrow), and a largely unstructured C terminus (red hollow arrow).

(E) Phylogenetic and localization analysis of Arl LSPs. The best Bayesian topology is shown with RAxML bootstrap (RB) and IQ-Tree rapid bootstrap (IB) support mapped. Important node support is shown in the order (Bayesian posterior probability/RB/IB), while internal node support is denoted by symbols per figure legend. Scale bar represents number of substitutions per site. ArlX LSP localization in *T. gondii* is depicted in the right panels. Intracellular parasites, each line with a different Arl LSP C-terminally tagged with a 3xHA tag, were stained with α-HA antibodies (colored yellow in the merge); parasites were outlined using α-Gap45 (an IMC marker, shown in magenta). Parasite nuclei were stained with DAPI (blue in the merge). Note the distinct localization pattern of each Arl LSP. Scale bar represents 5 μm.

ARF family G proteins, and their GAP and GTPase effector protein (GEF) regulators (Figure S1, Data S2). Overall, we identified 18 such paralogs in Apicomplexa and their relatives; the presumed patterns of gain and loss for which is summarized in Figure 1B.

SNAREs

Soluble *N*-ethylmaleimide-sensitive factor attachment receptor proteins (SNAREs) are coiled-coil proteins, often membrane-associated, that function in vesicle membrane fusion.[24] As expected, we identified homologs of the Qa, Qb, Qc, and R SNAREs across our study taxa (Figure S1, Data S1). There was a clear duplication of Stx12, giving rise to a myzozoan Stx12B paralog (Figure S2C). Likewise, we identified duplications of the R SNAREs VAMP7 (in Myzozoa, Figure S2K) and Ykt6 (in the apicomplexan-chromerid ancestor) (Figure S2L). The presence of Qbc SNAREs in Apicomplexa and sparsely across our study dataset (Figure S1, Data S2) is consistent with the ancient origin of this SNARE family and raises questions about the relationships of the Qb and Qc domains with respect to the other sub-families. The Qb domain is most closely related to NPSN (Figure S2H), and our data raise the intriguing possibility of a close evolutionary link between the Qc domain and SYP7 or Use1 (Figure S2I). Although it did not meet our criteria for an LSP, there was also a clear duplication of the Qa SNARE StxPM in hematozoans (Figure S2B).

Rab GTPases

Rabs are small (~200 amino acid) GTPases from the Ras superfamily that function in membrane trafficking and a variety of other cellular functions.[25] Overall, our results confirm the previously reported relationships between Rabs, including the overall division into endo/exocytic clades (Figures S2M and S2N, Data S1).[5] We confirm the presence and taxonomic distribution of several previously reported Rab LSPs (Figure 1B): Rab1A, present across SAR as well as the cryptophyte *Guillardia theta* (Figures S1 and S2O);[26] Rab11B, an alveolate-specific Rab11 paralog (Figures S1 and S2R);[27] Rab5C, a myzozoan-specific Rab5 paralog (Figures S1 and S2Q); and Rab5B, which is known as an atypical Rab5-like protein that we confirm here is conserved across alveolates (Figures S1 and S2Q).[28] Additionally, we report the presence of two previously unreported Rab LSPs. Rab1K is a further duplication of Rab1 that is restricted to chromerids, dinoflagellates, and coccidian apicomplexans closely related to *T. gondii* (Figures 1B, S1, and S2O). RabX1 is a myzozoan duplication of RabL2/RTW (Figures 1B, S1, and S2S).

TBC RabGAPs

The Tre-2/Bub-2/Cdc 16 (TBC) proteins are a diverse family of RabGAPs unified by the presence of a TBC domain. Overall, our results confirm the previously reported relationships between TBCs (Figures S2T and S2U, Data S1).[7] We identify five TBC LSPs, simply termed TBC-X1 through TBC-X5 (Figures 1B and S1). TBC-X2 groups with previously reported archaeplastid-specific TBC-PI proteins (Figure S2W) suggest a more complex origin for this group. TBC-X1, 3, 4, and 5 clades instead represent alveolate-specific duplications of TBC-Q (Figure S2X). Finally, a group of previously reported proteins containing both

an ArfGEF Sec7 and TBC domain (TBS proteins)[29] are confirmed here to be restricted to alveolates, with analogous proteins present in the haptophyte *Emiliania huxleyi* (Figures 1B, S2T–S2V, and S3L).[9]

ARF family G proteins

Like Rabs, ADP-ribosylation factor (ARF) family proteins, including ARF, ARF-like (Arl), and Sar proteins, are members of the Ras superfamily.[30,31] We identified three Arl LSPs, simply termed ArlX1 (conserved in alveolates and the rhizarian *Bigelowiella natans*), ArlX2 (found only in apicomplexans), and ArlX3 (present in chromerids and apicomplexans but absent from cryptosporidians, Figure 1B, Data S2). While *T. gondii* ArlX1 (TgArlX1) and TgArlX2 are similar in size to other canonical Arl homologs (~200 amino acids), TgArlX3 is almost three times the length with the canonical Arf domain split into two (Figure 1C). Molecular modeling (STAR Methods) suggests the presence of additional N-terminal helices, an internal loop between the canonical Arf folds, and an unstructured C terminus (Figure 1D). Despite extensive rounds of phylogenetic analysis (Data S1, Figures S3A–S3J), we were unable to determine a clear origin for all three ArlX proteins. ArlX1 is most likely a duplication of Arl16, while ArlX2 appears similar to the clade of Arl6 and Arl8; ArlX3, sequences of which are larger and more divergent than most Arl proteins, could not be resolved as related to any particular pan-eukaryotic Arl subfamily (Figure 1E). Its origins remain unclear. Despite the presence of three novel Arl proteins, there were no LSPs present for either ArfGEF or ArfGAP families (Figures S1 and S3K–S3M, Data S1); other regulators may govern these Arls.

Molecular characterization of Arl LSPs in *Toxoplasma gondii*

Molecular characterization of some SNARE and Rab proteins has been performed in *Toxoplasma*[32–34]; see Data S1.8. Furthermore, co-regulation analysis did demonstrate limited relationships between the expression of the LSPs (Figure S4, Data S1.7). However, to date there has been no systematic analysis of Arls in Apicomplexa. Therefore, we sought to characterize these three Arl LSPs using the model apicomplexan *T. gondii*. Using ligation-independent cloning (LIC) tagging, we created cell lines expressing each Arl LSP C-terminally tagged with a 3x-HA epitope tag (Figures 1E, S5, and S6).

ArlX1 localization varied but consistently appeared as a single punctum at the extreme apical end of intracellular tachyzoites, as well as dotted throughout the cell periphery (Figures 1E, S6A, and S6B). Signal was frequently observed in the basal body and throughout the intravacuolar network (Figure S6A). ArlX2 displayed an indistinct localization pattern, presenting as a sequence of punctate dots distributed throughout the entirety of the cell (Figure 1E). Lastly, ArlX3 appeared concentrated apical to the nucleus, in the region known to be occupied by the Golgi.[35] To further explore ArlX3 localization, we transiently transfected plasmids encoding fluorescently tagged markers: P30-GFP-HDEL, which labels the ER,[36] and ERD-GFP (*cis*-Golgi), GRASP-RFP (*cis*-Golgi), and GalNAc-YFP (*trans*-Golgi), which primarily label the Golgi.[35,37–39] There was little overlap with the ER marker but varying degrees of overlap with each of
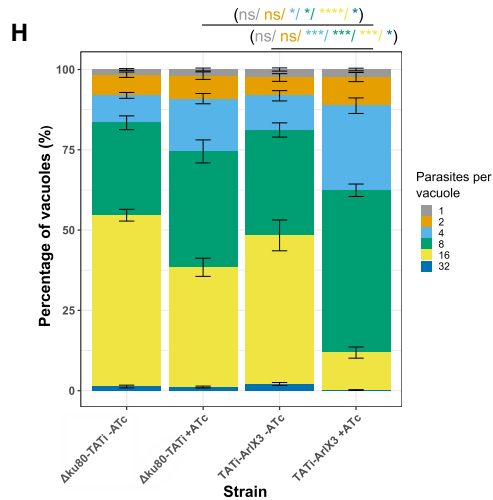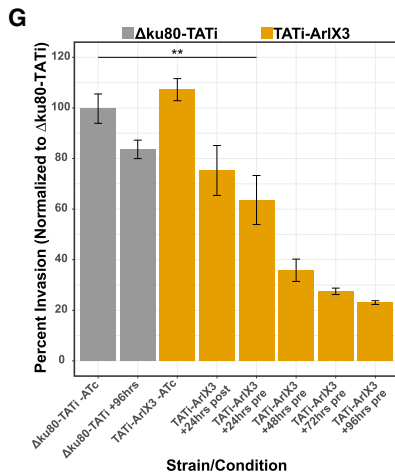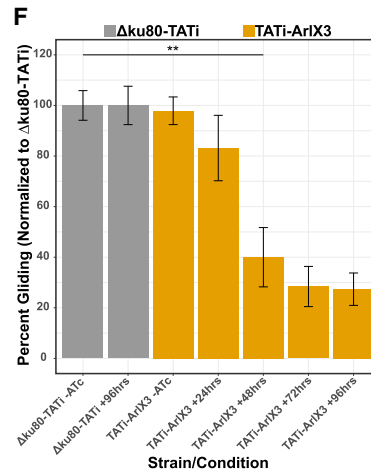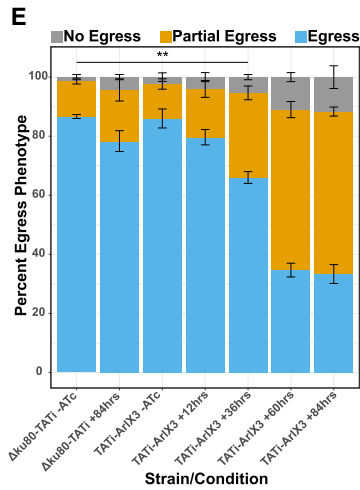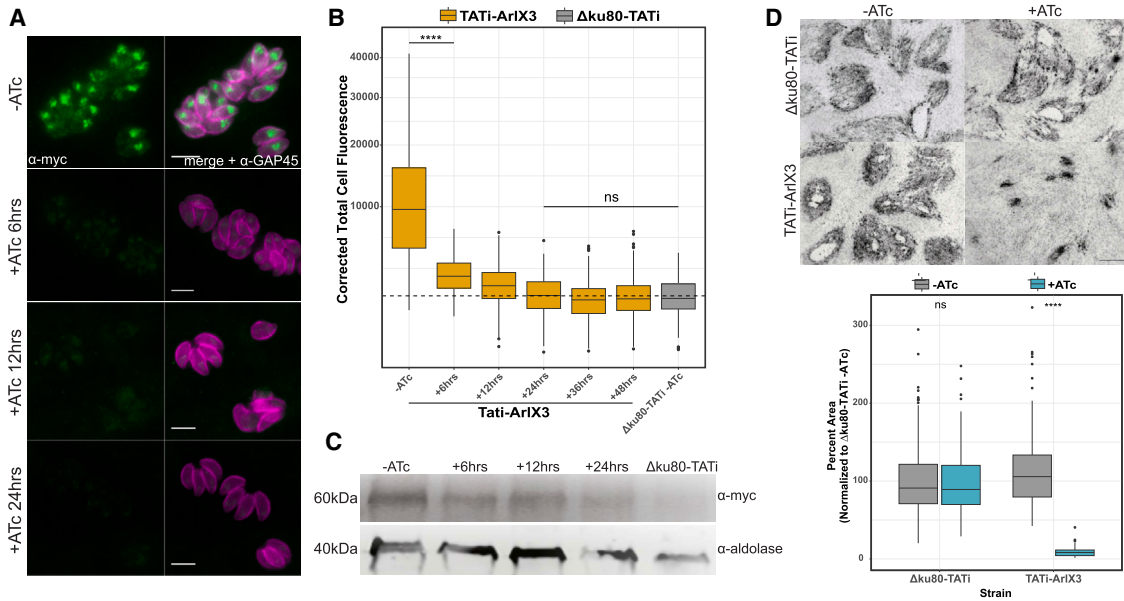
the three Golgi markers (Figure S6C), with GalNac being the marker with the strongest colocalization, suggesting that ArlX3 localizes to the *trans*-Golgi. Immunoelectron microscopy validates this localization and also localizes ArlX3 in vesicles and micronemes (Figure S6D).

Next, we disrupted *arlX1*, *arlX2*, or *arlX3* using CRISPR-Cas9 and investigated effects on the secretory organelles. (Data S1, Figures S6E and S7). While disruption of *arlX3* led to the defects in microneme and rhoptry biogenesis, Golgi, and endosomes (Figure S7), no defects were apparent for *arlX1* and *arlX2*. Furthermore, isolation of null mutants for *arlX1* and *arlX2* was possible, and no extreme growth defect could be observed. (Data S1, Figure S8) Overall, neither *arlX1* or *arlX2* disruption had a strong impact on the lytic cycle of *T. gondii* during the asexual stage, and both strains could be maintained in culture indefinitely (Figure S8). In contrast, no null mutant for *arlX3* could be isolated.

Creation of an inducible ArlX3 knockdown line

As our previous attempts to create a straight knockout line for ArlX3 failed, we attempted an inducible knockdown approach using the TATi system.[40] To this end, we constructed a TetO7-myc-pSag1-ArlX3 line, hereafter referred to as ArlX3-iKD, in which ArlX3 transcription is switched off by the addition of anhydrotetracycline (ATc; Figure S9). The localization of ArlX3-iKD remained consistent with alternative endogenously tagged versions, such as ArlX3-HA (Figures 2A and 1E). Quantitative immunofluorescence assay (IFA) and western blot analysis demonstrate tight ATc-mediated regulation of ArlX3, with significant downregulation as soon as 6 h and only background expression levels 24 h post induction (Figures 2A–2C and S9D).

As an initial characterization of our ArlX3-iKD line, we performed plaque assays, which assess the fitness of the parasite to carry out the lytic cycle and form clearing zones on human foreskin fibroblast monolayers. While the parental parasites grew indistinguishably in the presence or absence of ATc, growth of ArlX3-iKD was almost completely abrogated in the presence of ATc (Figure 2D). We carried out further assays to assess the ability of ArlX3-iKD parasites to egress, glide, invade, and replicate in the presence/absence of ATc. While parental parasites were unaffected by the presence of ATc, ArlX3-iKD parasites show a time-dependent decrease in their ability to carry out each of these lytic cycle steps, which, with the exception of cell division, depend on the biogenesis of secretory organelles[41] (Figures 2E–2H).

ArlX3 knockdown results in mislocalization of microneme and rhoptry cargo

As ArlX3-iKD impaired parasites in each step of the lytic cycle (Figures 2E–2G), we examined the apical secretory organelles, i.e., the micronemes and rhoptries, which play key roles in egress, gliding, and invasion.[42–45]

While parental parasites showed almost exclusively apical localization for each of the four microneme cargo proteins studied in the presence/absence of ATc, ArlX3-iKD parasites showed a time-dependent increase in cargo mislocalization (Figures 3A–3E and S9E). We noted three distinct patterns for mislocalized cargo: "vesicular," with punctate signal throughout the cell, "apical," with a clear punctum at the apical tip of the cell, and "basal body/extracellular (BB/E)," with signal concentrated within the basal body (indicated with a white arrow in the figure) or diffusely in the parasitophorous vacuole or both (Figure 3A). Interestingly, each cargo protein appeared to mislocalize in a distinct manner. AMA1 adopted a mainly apical signal (Figure 3B), M2AP mainly vesicular (Figure 3C), MIC3 overwhelmingly BB/E (Figure 3D), and MIC4 showed an approximately equal mix of all three patterns (Figure 3E). In each case though, mislocalization was moderate following 24 h of induction, increasing sharply with 48 h induction, and then a gradual increase through 96 h.

We observed a similar pattern with rhoptry markers (Figures 3F–3H and S9E). In both ROP2/3/4 and ROP5 markers, there was no clear preference for one pattern over another, and we observed similar temporal dynamics upon ArlX3 knockdown as for microneme cargoes (Figures 3G and 3H). As a control, we also studied the effect of ArlX3-iKD on the mitochondrion, which showed no defect even after 96 h (Figures 3I and 3J).

In summary, this characterization corresponded well to the data obtained in the Cas9 experiments mentioned above (see Figure S7).

ArlX3 knockdown affects the Golgi and early secretory system

As ArlX3 is localized to the Golgi (Figure S6C) and ArlX3-iKD results in cargo trafficking defects (Figure 3), we investigated the role of ArlX3-iKD on the Golgi itself. We first confirmed the close apposition of ArlX3 with the Golgi markers GRASP-RFP (*cis*-Golgi) and GalNAc-YFP (*trans*-Golgi), noting that the signal overlap appeared more dramatic with the latter (Figures S10A

Figure 2. ArlX3-iKD impairs each step of the lytic cycle
This figure summarizes the effects of TgArlX3-iKD on the *T. gondii* lytic cycle.
(A) ATc induction causes a time-dependent decrease in ArlX3 signal. Scale bar represents 10 μm.
(B) Background-normalized quantification of ArlX3 levels under ATc induction from 3 independent biological replicates; dotted line represents background signal. Note that signal intensity by 24 h post induction is not significantly different from the parental (Δku80-TATi) line. In this, and all subsequent bar graphs, the first instance of significant difference from controls is indicated. ns: non-significant differences and ****p < 0.0001.
(C) Western blot depicting downregulation of ArlX3 expression in parasites induced with ATc for the indicated times. Aldolase was employed as loading control. Longer time points are shown in Figure S9D.
(D) Plaque assay demonstrating the marked impact of ATc on TgArlX3-iKD parasite growth, with quantification shown below.
(E–G) TgArlX3-iKD impairs parasite egress (E), gliding (F), and invasion (G). In each case, the addition of ATc results in no significant difference in parental parasites but causes a time-dependent decrease in the ability of TgArlX3-iKD parasites to complete each lytic cycle step.
(H) Replication assay showed a slight delay in growth in ArlX3-KD parasites. A t test was performed comparing vacuoles with the same number of parasites. The significance of each parasite number vacuole is represented in the same color as its block in the stack bar graph. ns = not significant, *p < 0.05, **p < 0.01, ***p < 0.001, and ****p < 0.0001. Data are shown as mean ± SEM. All quantifications were obtained from 3 independent biological replicates.
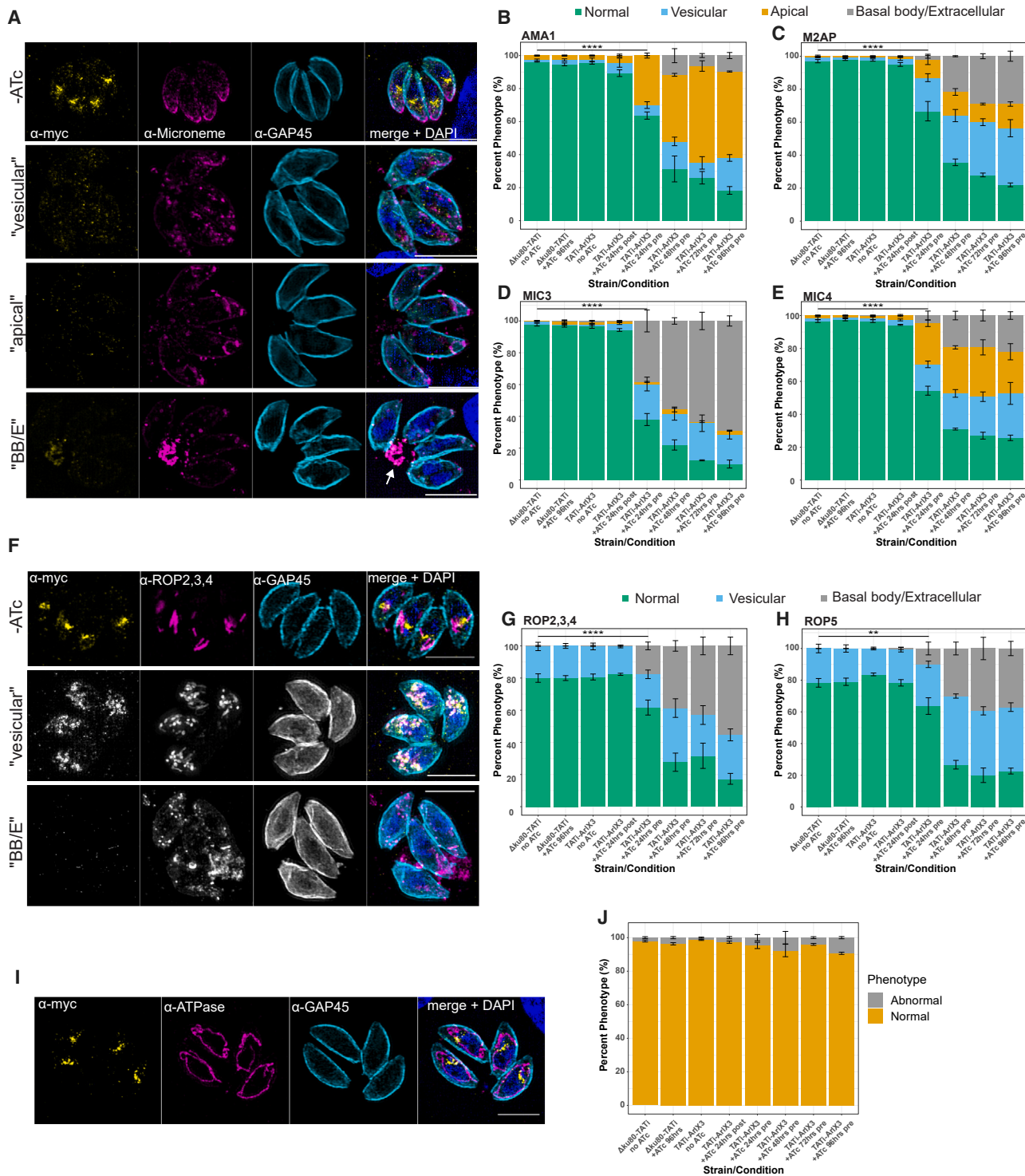
Figure 3. ArlX3-iKD results in mislocalization of microneme and rhoptry cargo
This figure shows the effect of TgArlX3-iKD on apical secretory organelles.
(A) In the absence of ATc, microneme protein staining adopts a characteristic apical pattern (top row). However, in the presence of ATc, the staining adopts one of three general patterns: scattered in puncta throughout the cell ("vesicular"), a single prominent dot at the apical tip ("apical"), or concentration in the basal body (white arrow), parasitophorous vacuole, or beyond ("BB/E"). Scale bar represents 5 μm (B–E) Quantification of staining patterns for the microneme proteins AMA1 (B), M2AP (C), MIC3 (D), and MIC4 (E) from 3 independent biological replicates. Note the preference for apical and BB/E staining with AMA1 and MIC3, respectively.

(legend continued on next page)

and S10B). While ArlX3-iKD had no apparent effect on GRASP-RFP localization (Figure S10A), by 48 h post induction, the GalNAc-YFP signal appeared aberrant (Figure S10B), suggesting that ArlX3 might act at the *trans*-Golgi to traffic material to the secretory organelles.

To test this hypothesis, we wished to analyze the effect of ArlX3 depletion on the localization of the cytosolic dynamin-like protein B (DrpB)[41] and the transmembrane cargo protein sortilin (SORTLR), which are required for trafficking of micronemal and rhoptry proteins from the *trans*-Golgi via early endosome-like compartment (ELC) to their final destination.[46] SORTLR was C-terminally tagged with YFP (Figure 4). As expected, in non-induced parasites, ArlX3 signal overlaps with that of YFP (Pearson correlation $r = 0.77 \pm 0.07$), confirming that ArlX3 primarily localizes at the *trans*-Golgi (Figure 4A). However, upon induction of ArlX3 knockdown, SORTLR signal ceased to be restricted to the Golgi-ELC area, appearing fragmented by 48 h post induction with ATc (Figures 4A–4C), while DrpB shows also a more cytosolic localization at a time comparable to the observed defects on micronemes and rhoptries.

These results are confirmed by transmission electron micrographs on ArlX3-iKD parasites in the presence/absence of ATc, which show a lack of recognizable stacked *trans*-Golgi in the presence of ATc (Figure 4D). We therefore conclude that ArlX3 is required for the trafficking of micronemal and rhoptry material from the *trans*-Golgi to the unique secretory organelles.

DISCUSSION

In this study, we have confirmed the presence of 18 LSPs in Apicomplexa and related taxa, and we explored the role of one LSP, ArlX3, in membrane trafficking in *T. gondii*. These results suggest a previously unexplored wealth of unique trafficking factors in a lineage of important eukaryotic parasites, with implications for understanding apicomplexan cell biology and eukaryotic evolution.

Although some LSPs, such as Rabs 1A, 5B, 5C, and 11B and the TBS proteins have been reported previously,[26–29] their unique phylogenetic relationship compared to other trafficking factors was not fully explored. We report here the presence of multiple additional LSPs, including examples from the Arl, Rab, SNARE, and TBC families (Figures 1B and S1). Most saliently, we have shown that ArlX3 plays an important role in *T. gondii* tachyzoites, as ArlX3-iKD abrogates parasite growth (Figure 2D). While the overall morphology of the parasites remains intact, we found that upon downregulation of ArlX3, the parasites replicated slightly slower and failed to form the micronemes and rhoptries, leading to parasites being unable to egress, glide, or invade the host cell (Figures 2E–2H, 3, and S9). This phenotype is very similar to a phenotype observed upon disruption of the dynamin-related protein B (DrpB[41]). Although some previous studies have noted the existence of alternative fates for mislocal-

ized cargoes,[47,48] quantification of mislocalization frequently follows a binary approach (i.e., [mis]localized). In terms of micronemes, the vesicular staining may result from a failure to properly traffic microneme protein-containing vesicles, a failure of microneme recycling following endodyogeny, or some other defect. Similarly, the basal body staining may represent a recycling failure, while extracellular staining likely represents aberrant microneme protein inclusion in the "default constitutive" dense granule secretion pathway.[49,50] The apical signal is enigmatic; it was previously proposed to represent a novel trafficking pathway to a subgroup of apical micronemes.[47,51] However, this is inconsistent with the observation that TgSORTLR, responsible for forward translocation of microneme and rhoptry cargo from the TGN, also results in apical staining (see for example Figure 4 in Sloves et al.).[46] Although some vesicular rhoptry marker staining is always observed (Figures 3F–3H), likely representing nascent rhoptries forming from a Rab5A-positive compartment,[48] the ratio is increased in ArlX3-iKD parasites, suggesting a defect in trafficking, fusion, or both.

Compared with Rab5A/C, in which only some microneme cargo proteins were mislocalized with the overexpression of a dominant-negative (DN) form of either Rab,[28] all four cargo proteins tested here were mislocalized with ArlX3-iKD (Figures 3B–3E). This included proteins that had a normal localization with DN Rab5A/C, such as AMA1 and M2AP, as well as a protein that was mislocalized (MIC3). This may indicate that ArlX3 acts upstream of Rab5A/C in forward secretory trafficking or that it functions in multiple pathways. The blanket effect of both Rab5A/C and ArlX3 disruption on rhoptry cargo localization supports distinct pathways for microneme and rhoptry biogenesis.

Our quantification of microneme marker mislocalization (Figures 3B–3E) suggests that these proteins are differentially capable of unassisted forward trafficking and of entering alternate trafficking pathways. It also supports the idea that ArlX3 is involved in the forward trafficking of diverse microneme proteins.

Although our study suggests a role for ArlX3 in post-Golgi trafficking in apicomplexans, the exact function of ArlX3 remains unclear. This is in part hampered by the lack of a clear origin for ArlX3 (Figures 1 and S3, Data S1). In cases where an apicomplexan LSP has a clear origin, for example both Rab5C and 11B, the function has remained similar to that of its pan-eukaryotic paralog.[27,28] In addition, Arl biology remains comparatively understudied, with diverse functions in membrane trafficking, cytoskeletal organization, and ciliogenesis/intraflagellar transport posited for various family members.[31] The notion that ArlX3-iKD impairs trafficking is suggested by the extensive mislocalization of microneme and rhoptry proteins (Figure 3). In addition, our observation of a more general disruption on Golgi/ELC morphology (Figures 4 and S10) bears striking similarity to disruption of another TGN resident trafficking protein in *T. gondii*, Stx6.[52] We have recently published an extensive model for trafficking in *T. gondii*[18]; here, we suggest the possible

(F) Staining patterns for rhoptry proteins, as in (A); note the absence of apical staining. Scale bar represents 5 μm.

(G and H) Quantification of staining patterns for the rhoptry proteins ROP2, 3, and 4 (polyclonal) and ROP5 from 3 independent biological replicates.

(I) Example images of "normal" localization of the mitochondrion (ATPase). The classic "lasso" is depicted, although other morphologies have also been described in wild-type parasites.

(J) Quantification of mitochondria staining from 3 independent biological replicates. **p < 0.01 and ****p < 0.0001. Data are shown as mean ± SEM.
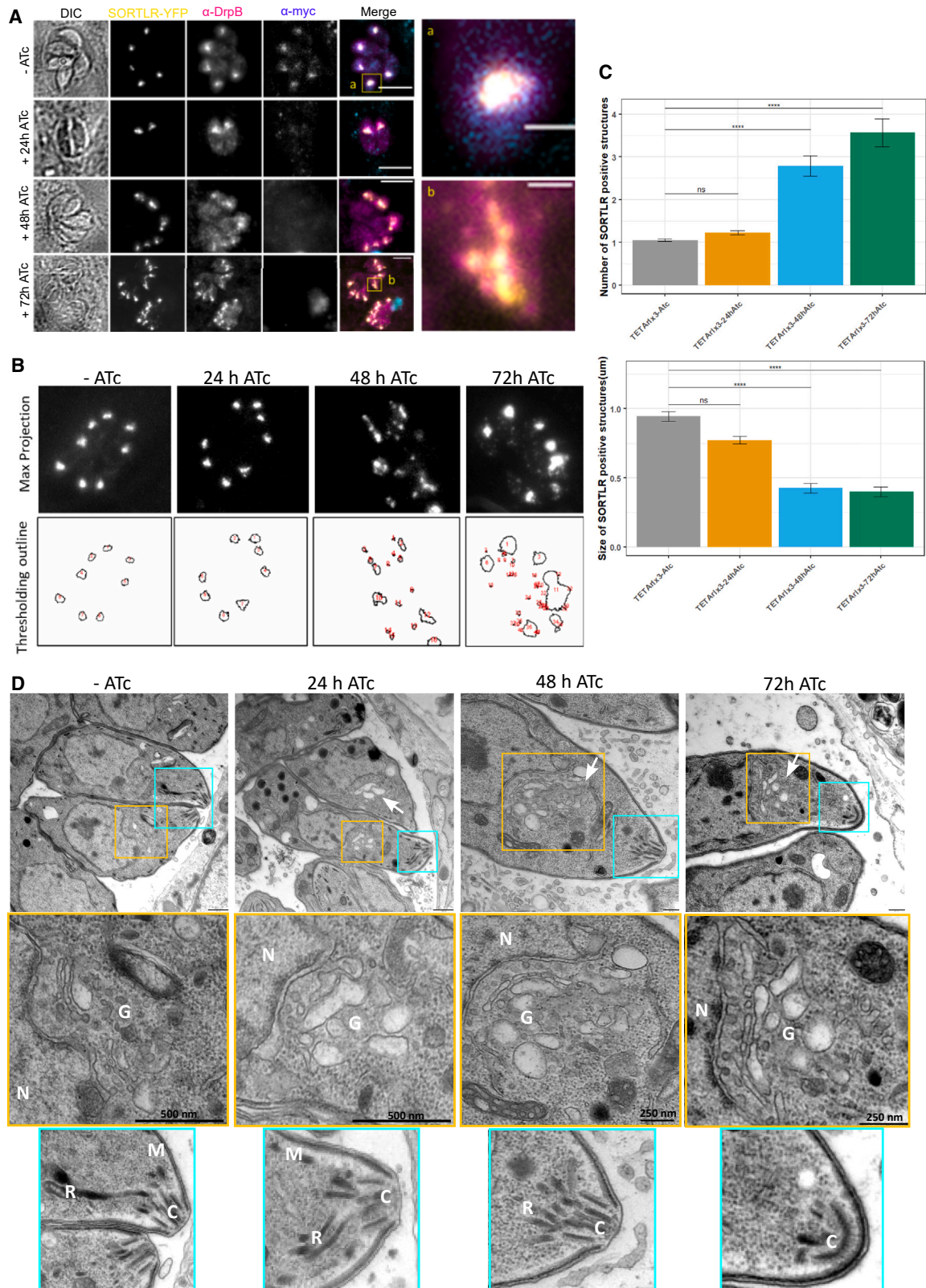
(legend on next page)

inclusion of ArlX3 (Figure 5). Future studies should elaborate the precise role of ArlX3 in the apicomplexan MTS.

A larger question pertains to the evolutionary cell biological implications of the LSPs themselves. We have previously argued that the OPH, which was conceived to explain the proliferation of distinct organelles during the FECA-LECA transition, is just as relevant to modern-day eukaryotes.[13] In this view, continued paralogous duplication and diversification of trafficking factors would allow for the emergence of additional unique organelles in eukaryotic lineages. The expectation under this model is therefore that the LSP should be taxonomically restricted to only those lineages in which the unique structure or organelle is present. This is supported by previous studies of some of the LSPs identified here. Rab5C, which we confirm is present across the Myzozoa (Data S2, Figures 1B, S1, and S2Q), is involved in trafficking to apical secretory organelles,[28] which are conserved across this group.[19] Rab11B, which we confirm is conserved across alveolates (Data S2, Figures 1B, S1, and S2R), is involved in trafficking to the IMC in *T. gondii*,[27] which is homologous to the alveoli of all alveolates.[20] Although less clear cut, molecular characterizations of other LSPs in recent studies, including Rab1A, Rab5B, Stx12B, and Ykt6B, appear to also fit the general pattern of function relating to lineage-specific cellular structures (Data S1). Additionally, our results regarding ArlX3 also follow this pattern. ArlX3 is restricted to myzozoans (Data S2, Figures 1B, S1, and S3) and, like Rab5C, plays a role in proper localization of microneme and rhoptry cargoes (Figure 3). Hence, our results lend weight to the idea that the OPH continues to operate in extant eukaryotes, giving rise to unique organelles not conserved across eukaryotic diversity.

In this study, we have confirmed the presence of 18 LSPs in Apicomplexa and their close relatives and showed that one such LSP, ArlX3, plays an important role in asexual *T. gondii* tachyzoites. These results have important implications not only for apicomplexan cell biology but for understanding the conservation and emergence of eukaryotic trafficking factors. Future studies should investigate the correlation between phylogenetic distribution and function of trafficking factors more closely. Our results provide a list of potential targets for those working in apicomplexan cell models and, on a more fundamental level, a general template for uncovering and exploring novel cell biology applicable to any eukaryote.

Limitations of the study
While this study provides valuable insights into the presence of LSPs in Apicomplexa and their role, it is essential to consider the limitations of the study.

We acknowledge that the exact function of ArlX3 remains unclear. Without a detailed understanding of the molecular function of ArlX3, it is challenging to draw definitive conclusions about its role in membrane trafficking. Indeed, this study relies on morphological changes in the parasites, such as altered Golgi/ELC morphology and defects in microneme and rhoptry formation, as indicators of ArlX3 function. However, they may not always correlate directly with specific molecular functions. Moreover, while we identified 18 LSPs in Apicomplexa, the inclusion of new 'omics information from members of Alveolata not sampled in this study could change inferences regarding the precise timing of the protein acquisitions or could identify further examples. It would undoubtedly provide more detail regarding the precise patterns of gains and losses of these LSPs in organisms with important medical and/or environmental importance.

In conclusion, while the study makes significant contributions to our understanding of LSPs in Apicomplexa and highlights the potential role of ArlX3, researchers and readers should be aware of these limitations and consider them when interpreting the results. Further research and validation are needed to enhance the robustness of the findings and broaden the applicability of the conclusions to a broader context.

STAR★METHODS

Detailed methods are provided in the online version of this paper and include the following:

- KEY RESOURCES TABLE
- RESOURCE AVAILABILITY
  - Lead contact
  - Materials availability
  - Data and code availability
- METHOD DETAILS
  - Homology searching and phylogenetic analysis
  - Protein structural prediction
  - Analysis of gene co-expression
  - Parasite and host cell culture
  - Genomic DNA isolation, cloning, and PCR
  - Transfection of parasites
  - Immunofluorescence assays
  - Plaque assay
  - Gliding assay
  - Invasion-replication assay
  - Egress assay
  - Western blotting and protein detection
  - Structured illumination microscopy (SIM)

Figure 4. ArlX3-iKD impacts the organization of the Golgi and ELC
This figure shows the effect of the absence of ArlX3 in Golgi and ELC stability.
(A) Images depicting ArlX3-iKD-SORTLR-YFP parasites ± ATc for the indicated time points and stained with α-myc and α-DrpB antibodies. Both Sortilin and DrpB are markers for Golgi. Insets show the merged image of all 3 channels where there is colocalization of ArlX3 with the Golgi markers in non-induce parasites in a defined area that is the Golgi. After 72 h of induction, the Golgi seemed to fragment, and several vesicles were observed.
(B) Analysis of the vesicles with SORTLR signal. Representative images of the SORTLR channel and the outline of the threshold applied with Fiji are shown.
(C) Bar graphs showing the quantification of vesicles (representative images in B), their size, and the average intensity of vesicles analyzed from 3 independent biological replicates. Data are shown as mean ± SEM.
(D) Representative EM images of parasites induced with ATc. White arrows indicate fragmented Golgi vesicles. Insets show a closer image of the Golgi area (yellow) or the secretory organelles (blue). N: nucleus; G: Golgi; M: micronemes; R: rhoptry; C: conoid.
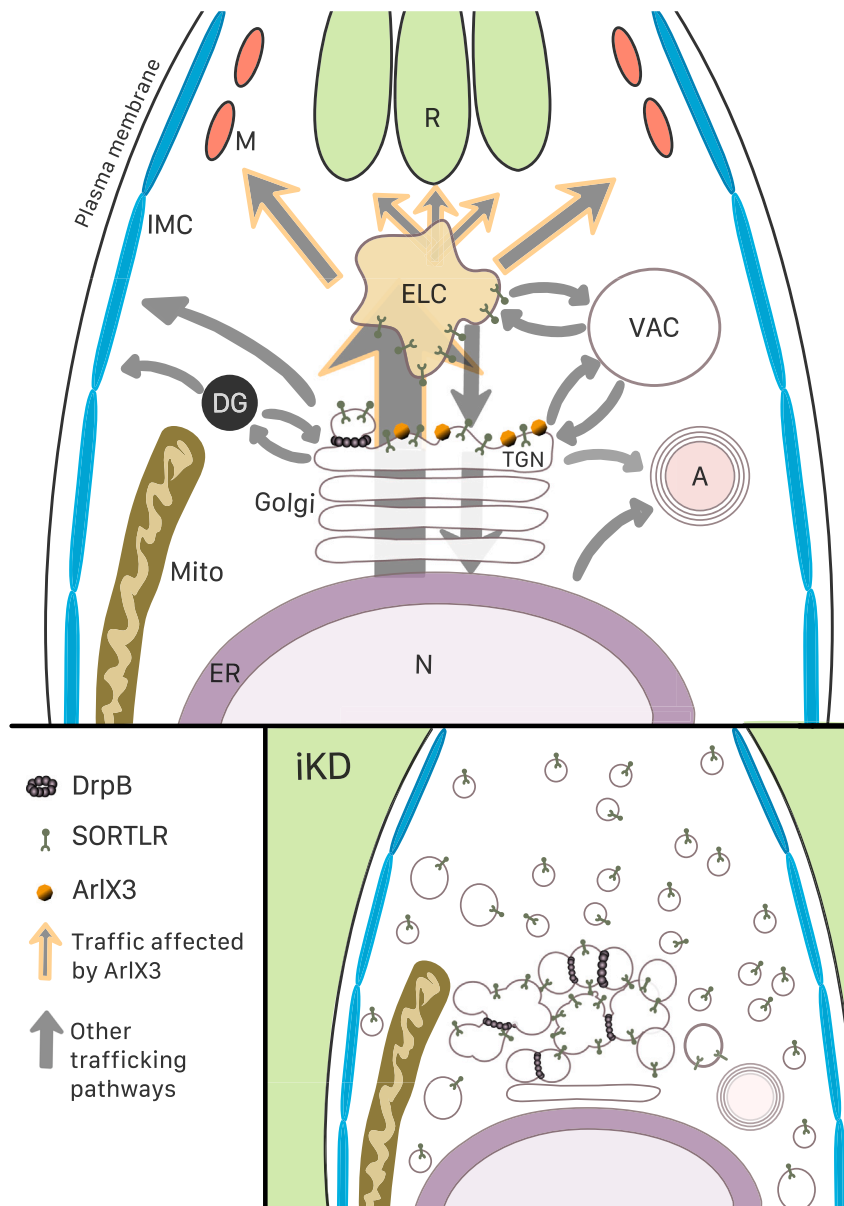
Figure 5. A comprehensive model of *T. gondii* membrane trafficking

This figure outlines a current view of *T. gondii* membrane trafficking, including insights from this study regarding the localization and possible function of ArlX3. In the main panel, highlighted arrows show traffic routes toward micronemes and rhoptries where ArlX3 is involved. In the lower panel, depletion of ArlX3-KD (iKD) leads to the disruption of the *trans*-Golgi. M: micronemes, R: rhoptries, IMC: inner membrane complex, ELC: endosomal-like compartment, VAC: plant-like vacuole, DG: dense granules, TGN: *trans*-Golgi network, A: apicoplast, Mito: mitochondria, ER: endoplasmic reticulum, N: nucleus.

- ○ Electron microscopy
- ○ Quantitative fluorescence microscopy and image analysis
- ● QUANTIFICATION AND STATISTICAL ANALYSIS

SUPPLEMENTAL INFORMATION

ACKNOWLEDGMENTS

AUTHOR CONTRIBUTIONS

C.M.K. designed and interpreted bioinformatics data, designed and performed part of the cell biology experiments in Tg and data analysis, and co-wrote the manuscript. E.J.R. designed and performed part of the cell biology experiments in Tg and data analysis and co-wrote the manuscript, and T.M. performed the gene co-regulation analysis. A.K. performed electron

microscopy (EM) imaging and analysis, and L.L. helped with imaging analysis and performed cryo-immuno-EM. A.P. designed and helped in the interpretation of the gene co-regulation analysis. J.B.D. aided in the overall project design and bioinformatics data interpretation and co-wrote the manuscript. M.M. aided in overall project design, designed cell biology experiments in Tg, assisted in data interpretation, and co-wrote the manuscript.

DECLARATION OF INTERESTS

REFERENCES

1. More, K., Klinger, C.M., Barlow, L.D., and Dacks, J.B. (2020). Evolution and Natural History of Membrane Trafficking in Eukaryotes. Curr. Biol. *30*, R553-r564. https://doi.org/10.1016/j.cub.2020.03.068.

2. Bonifacino, J.S., and Glick, B.S. (2004). The mechanisms of vesicle budding and fusion. Cell *116*, 153–166. https://doi.org/10.1016/s0092-8674(03)01079-1.

3. Klinger, C.M., Spang, A., Dacks, J.B., and Ettema, T.J.G. (2016). Tracing the Archaeal Origins of Eukaryotic Membrane-Trafficking System Building Blocks. Mol. Biol. Evol. *33*, 1528–1541. https://doi.org/10.1093/molbev/msw034.

4. Dacks, J.B., and Field, M.C. (2007). Evolution of the eukaryotic membrane-trafficking system: origin, tempo and mode. J. Cell Sci. *120*, 2977–2985. https://doi.org/10.1242/jcs.013250.

5. Elias, M., Brighouse, A., Gabernet-Castello, C., Field, M.C., and Dacks, J.B. (2012). Sculpting the endomembrane system in deep time: high resolution phylogenetics of Rab GTPases. J. Cell Sci. *125*, 2500–2508. https://doi.org/10.1242/jcs.101378.

6. Vargová, R., Wideman, J.G., Derelle, R., Klimeš, V., Kahn, R.A., Dacks, J.B., and Eliáš, M. (2021). A Eukaryote-Wide Perspective on the Diversity and Evolution of the ARF GTPase Protein Family. Genome Biol. Evol. *13*, evab157. https://doi.org/10.1093/gbe/evab157.

7. Gabernet-Castello, C., O'Reilly, A.J., Dacks, J.B., and Field, M.C. (2013). Evolution of Tre-2/Bub2/Cdc16 (TBC) Rab GTPase-activating proteins. Mol. Biol. Cell *24*, 1574–1583. https://doi.org/10.1091/mbc.E12-07-0557.

8. Schlacht, A., Mowbrey, K., Elias, M., Kahn, R.A., and Dacks, J.B. (2013). Ancient complexity, opisthokont plasticity, and discovery of the 11th subfamily of Arf GAP proteins. Traffic *14*, 636–649. https://doi.org/10.1111/tra.12063.

9. Pipaliya, S.V., Schlacht, A., Klinger, C.M., Kahn, R.A., and Dacks, J. (2019). Ancient complement and lineage-specific evolution of the Sec7 ARF GEF proteins in eukaryotes. Mol. Biol. Cell *30*, 1846–1863. https://doi.org/10.1091/mbc.E19-01-0073.

10. Spang, A., and Ettema, T.J.G. (2016). Microbial diversity: The tree of life comes of age. Nat. Microbiol. *1*, 16056. https://doi.org/10.1038/nmicrobiol.2016.56.

11. Eme, L., Tamarit, D., Caceres, E.F., Stairs, C.W., De Anda, V., Schön, M.E., Seitz, K.W., Dombrowski, N., Lewis, W.H., Homa, F., et al. (2023). Inference and reconstruction of the heimdallarchaeial ancestry of eukaryotes. Nature *618*, 992–999. https://doi.org/10.1038/s41586-023-06186-2.

12. Dacks, J.B., and Field, M.C. (2018). Evolutionary origins and specialisation of membrane transport. Curr. Opin. Cell Biol. *53*, 70–76. https://doi.org/10.1016/j.ceb.2018.06.001.

13. Klinger, C.M., Ramirez-Macias, I., Herman, E.K., Turkewitz, A.P., Field, M.C., and Dacks, J. (2016). Resolving the homology-function relationship through comparative genomics of membrane-trafficking machinery and parasite cell biology. Mol. Biochem. Parasitol. *209*, 88–103. https://doi.org/10.1016/j.molbiopara.2016.07.003.

14. Marks, M.S., Heijnen, H.F.G., and Raposo, G. (2013). Lysosome-related organelles: unusual compartments become mainstream. Curr. Opin. Cell Biol. *25*, 495–505. https://doi.org/10.1016/j.ceb.2013.04.008.

15. Moore, R.B., Oborník, M., Janouskovec, J., Chrudimský, T., Vancová, M., Green, D.H., Wright, S.W., Davies, N.W., Bolch, C.J.S., Heimann, K., et al. (2008). A photosynthetic alveolate closely related to apicomplexan parasites. Nature *451*, 959–963. https://doi.org/10.1038/nature06635.

16. Oborník, M., Modrý, D., Lukeš, M., Cernotíková-Stříbrná, E., Cihlář, J., Tesařová, M., Kotabová, E., Vancová, M., Prášil, O., and Lukeš, J. (2012). Morphology, ultrastructure and life cycle of Vitrella brassicaformis n. sp., n. gen., a novel chromerid from the Great Barrier Reef. Protist *163*, 306–323. https://doi.org/10.1016/j.protis.2011.09.001.

17. Butterfield, E.R., Howe, C.J., and Nisbet, R.E.R. (2013). An analysis of dinoflagellate metabolism using EST data. Protist *164*, 218–236. https://doi.org/10.1016/j.protis.2012.09.001.

18. Besteiro, S., Klinger, C.M., Meissner, M., and Carruthers, V.B. (2020). Chapter 15 - Endomembrane trafficking pathways in Toxoplasma. In Toxoplasma Gondii, Third Edition, L.M. Weiss and K. Kim, eds. (Academic Press), pp. 705–741. https://doi.org/10.1016/B978-0-12-815041-2.00015-3.

19. Okamoto, N., and Keeling, P.J. (2014). The 3D structure of the apical complex and association with the flagellar apparatus revealed by serial TEM tomography in Psammosa pacifica, a distant relative of the Apicomplexa. PLoS One *9*, e84653. https://doi.org/10.1371/journal.pone.0084653.

20. Klinger, C.M., Nisbet, R.E., Ouologuem, D.T., Roos, D.S., and Dacks, J.B. (2013). Cryptic organelle homology in apicomplexan parasites: insights from evolutionary cell biology. Curr. Opin. Microbiol. *16*, 424–431. https://doi.org/10.1016/j.mib.2013.07.015.

21. Kuppannan, A., Jiang, Y.Y., Maier, W., Liu, C., Lang, C.F., Cheng, C.Y., Field, M.C., Zhao, M., Zoltner, M., and Turkewitz, A.P. (2022). A novel membrane complex is required for docking and regulated exocytosis of lysosome-related organelles in Tetrahymena thermophila. PLoS Genet. *18*, e1010194. https://doi.org/10.1371/journal.pgen.1010194.

22. Jiménez-Ruiz, E., Wong, E.H., Pall, G.S., and Meissner, M. (2014). Advantages and disadvantages of conditional systems for characterization of essential genes in Toxoplasma gondii. Parasitology *141*, 1390–1398. https://doi.org/10.1017/s0031182014000559.

23. Briquet, S., Gissot, M., and Silvie, O. (2022). A toolbox for conditional control of gene expression in apicomplexan parasites. Mol. Microbiol. *117*, 618–631. https://doi.org/10.1111/mmi.14821.

24. Han, J., Pluhackova, K., and Böckmann, R.A. (2017). The Multifaceted Role of SNARE Proteins in Membrane Fusion. Front. Physiol. *8*, 5. https://doi.org/10.3389/fphys.2017.00005.

25. Stenmark, H. (2009). Rab GTPases as coordinators of vesicle traffic. Nat. Rev. Mol. Cell Biol. *10*, 513–525. https://doi.org/10.1038/nrm2728.

26. Elias, M., Patron, N.J., and Keeling, P.J. (2009). The RAB family GTPase Rab1A from Plasmodium falciparum defines a unique paralog shared by chromalveolates and rhizaria. J. Eukaryot. Microbiol. *56*, 348–356. https://doi.org/10.1111/j.1550-7408.2009.00408.x.

27. Agop-Nersesian, C., Egarter, S., Langsley, G., Foth, B.J., Ferguson, D.J.P., and Meissner, M. (2010). Biogenesis of the inner membrane complex is dependent on vesicular transport by the alveolate specific GTPase Rab11B. PLoS Pathog. *6*, e1001029. https://doi.org/10.1371/journal.ppat.1001029.

28. Kremer, K., Kamin, D., Rittweger, E., Wilkes, J., Flammer, H., Mahler, S., Heng, J., Tonkin, C.J., Langsley, G., Hell, S.W., et al. (2013). An overexpression screen of Toxoplasma gondii Rab-GTPases reveals distinct transport routes to the micronemes. PLoS Pathog. *9*, e1003213. https://doi.org/10.1371/journal.ppat.1003213.

29. Mouratou, B., Biou, V., Joubert, A., Cohen, J., Shields, D.J., Geldner, N., Jürgens, G., Melançon, P., and Cherfils, J. (2005). The domain architecture

of large guanine nucleotide exchange factors for the small GTP-binding protein Arf. BMC Genom. *6*, 20. https://doi.org/10.1186/1471-2164-6-20.

30. Rojas, A.M., Fuentes, G., Rausell, A., and Valencia, A. (2012). The Ras protein superfamily: evolutionary tree and role of conserved amino acids. J. Cell Biol. *196*, 189–201. https://doi.org/10.1083/jcb.201103008.

31. Donaldson, J.G., and Jackson, C.L. (2011). ARF family G proteins and their regulators: roles in membrane transport, development and disease. Nat. Rev. Mol. Cell Biol. *12*, 362–375. https://doi.org/10.1038/nrm3117.

32. Bisio, H., Chaabene, R.B., Sabitzki, R., Maco, B., Marq, J.B., Gilberger, T.W., Spielmann, T., and Soldati-Favre, D. (2020). The ZIP Code of Vesicle Trafficking in Apicomplexa: SEC1/Munc18 and SNARE Proteins. mBio *11*, e0209220. https://doi.org/10.1128/mBio.02092-20.

33. Cao, S., Yang, J., Fu, J., Chen, H., and Jia, H. (2021). The Dissection of SNAREs Reveals Key Factors for Vesicular Trafficking to the Endosome-like Compartment and Apicoplast via the Secretory System in Toxoplasma gondii. mBio *12*, e0138021. https://doi.org/10.1128/mBio.01380-21.

34. Venugopal, K., and Marion, S. (2018). Secretory organelle trafficking in Toxoplasma gondii: A long story for a short travel. Int. J. Med. Microbiol. *308*, 751–760. https://doi.org/10.1016/j.ijmm.2018.07.007.

35. Pelletier, L., Stern, C.A., Pypaert, M., Sheff, D., Ngô, H.M., Roper, N., He, C.Y., Hu, K., Toomre, D., Coppens, I., et al. (2002). Golgi biogenesis in Toxoplasma gondii. Nature *418*, 548–552. https://doi.org/10.1038/nature00946.

36. Hager, K.M., Striepen, B., Tilney, L.G., and Roos, D.S. (1999). The nuclear envelope serves as an intermediary between the ER and Golgi complex in the intracellular parasite Toxoplasma gondii. J. Cell Sci. *112*, 2631–2638. https://doi.org/10.1242/jcs.112.16.2631.

37. Wojczyk, B.S., Stwora-Wojczyk, M.M., Hagen, F.K., Striepen, B., Hang, H.C., Bertozzi, C.R., Roos, D.S., and Spitalnik, S.L. (2003). cDNA cloning and expression of UDP-N-acetyl-D-galactosamine:polypeptide N-acetylgalactosaminyltransferase T1 from Toxoplasma gondii. Mol. Biochem. Parasitol. *131*, 93–107. https://doi.org/10.1016/s0166-6851(03)00196-8.

38. Pfluger, S.L., Goodson, H.V., Moran, J.M., Ruggiero, C.J., Ye, X., Emmons, K.M., and Hager, K.M. (2005). Receptor for retrograde transport in the apicomplexan parasite Toxoplasma gondii. Eukaryot. Cell *4*, 432–442. https://doi.org/10.1128/ec.4.2.432-442.2005.

39. Harper, J.M., Huynh, M.H., Coppens, I., Parussini, F., Moreno, S., and Carruthers, V.B. (2006). A cleavable propeptide influences Toxoplasma infection by facilitating the trafficking and secretion of the TgMIC2-M2AP invasion complex. Mol. Biol. Cell *17*, 4551–4563. https://doi.org/10.1091/mbc.e06-01-0064.

40. Meissner, M., Schlüter, D., and Soldati, D. (2002). Role of Toxoplasma gondii myosin A in powering parasite gliding and host cell invasion. Science *298*, 837–840. https://doi.org/10.1126/science.1074553.

41. Breinich, M.S., Ferguson, D.J.P., Foth, B.J., van Dooren, G.G., Lebrun, M., Quon, D.V., Striepen, B., Bradley, P.J., Frischknecht, F., Carruthers, V.B., and Meissner, M. (2009). A dynamin is required for the biogenesis of secretory organelles in Toxoplasma gondii. Curr. Biol. *19*, 277–286. https://doi.org/10.1016/j.cub.2009.01.039.

42. Carruthers, V.B., and Sibley, L.D. (1997). Sequential protein secretion from three distinct organelles of Toxoplasma gondii accompanies invasion of human fibroblasts. Eur. J. Cell Biol. *73*, 114–123.

43. Blader, I.J., Coleman, B.I., Chen, C.T., and Gubbels, M.J. (2015). Lytic Cycle of Toxoplasma gondii: 15 Years Later. Annu. Rev. Microbiol. *69*, 463–485. https://doi.org/10.1146/annurev-micro-091014-104100.

44. Kafsack, B.F.C., Pena, J.D.O., Coppens, I., Ravindran, S., Boothroyd, J.C., and Carruthers, V.B. (2009). Rapid membrane disruption by a perforin-like protein facilitates parasite exit from host cells. Science *323*, 530–533. https://doi.org/10.1126/science.1165740.

45. Gras, S., Jimenez-Ruiz, E., Klinger, C.M., Schneider, K., Klingl, A., Lemgruber, L., and Meissner, M. (2019). An endocytic-secretory cycle partic-
ipates in Toxoplasma gondii in motility. PLoS Biol. *17*, e3000060. https://doi.org/10.1371/journal.pbio.3000060.

46. Sloves, P.J., Delhaye, S., Mouveaux, T., Werkmeister, E., Slomianny, C., Hovasse, A., Dilezitoko Alayi, T., Callebaut, I., Gaji, R.Y., Schaeffer-Reiss, C., et al. (2012). Toxoplasma sortilin-like receptor regulates protein transport and is essential for apical secretory organelle biogenesis and host infection. Cell host & microbe *11*, 515–527. https://doi.org/10.1016/j.chom.2012.03.006.

47. Morlon-Guyot, J., Pastore, S., Berry, L., Lebrun, M., and Daher, W. (2015). Toxoplasma gondii Vps11, a subunit of HOPS and CORVET tethering complexes, is essential for the biogenesis of secretory organelles. Cell Microbiol. *17*, 1157–1178. https://doi.org/10.1111/cmi.12426.

48. Venugopal, K., Werkmeister, E., Barois, N., Saliou, J.M., Poncet, A., Huot, L., Sindikubwabo, F., Hakimi, M.A., Langsley, G., Lafont, F., and Marion, S. (2017). Dual role of the Toxoplasma gondii clathrin adaptor AP1 in the sorting of rhoptry and microneme proteins and in parasite division. PLoS Pathog. *13*, e1006331. https://doi.org/10.1371/journal.ppat.1006331.

49. Karsten, V., Qi, H., Beckers, C.J., Reddy, A., Dubremetz, J.F., Webster, P., and Joiner, K.A. (1998). The protozoan parasite Toxoplasma gondii targets proteins to dense granules and the vacuolar space using both conserved and unusual mechanisms. J. Cell Biol. *141*, 1323–1333. https://doi.org/10.1083/jcb.141.6.1323.

50. Chaturvedi, S., Qi, H., Coleman, D., Rodriguez, A., Hanson, P.I., Striepen, B., Roos, D.S., and Joiner, K.A. (1999). Constitutive calcium-independent release of Toxoplasma gondii dense granules occurs through the NSF/SNAP/SNARE/Rab machinery. J. Biol. Chem. *274*, 2424–2431. https://doi.org/10.1074/jbc.274.4.2424.

51. Matthiesen, S.H., Shenoy, S.M., Kim, K., Singer, R.H., and Satir, B.H. (2001). A parafusin-related Toxoplasma protein in Ca2+-regulated secretory organelles. Eur. J. Cell Biol. *80*, 775–783. https://doi.org/10.1078/0171-9335-00214.

52. Jackson, A.J., Clucas, C., Mamczur, N.J., Ferguson, D.J., and Meissner, M. (2013). Toxoplasma gondii Syntaxin 6 is required for vesicular transport between endosomal-like compartments and the Golgi complex. Traffic *14*, 1166–1181. https://doi.org/10.1111/tra.12102.

53. Donald, R.G., Carter, D., Ullman, B., and Roos, D.S. (1996). Insertional tagging, cloning, and expression of the Toxoplasma gondii hypoxanthine-xanthine-guanine phosphoribosyltransferase gene. Use as a selectable marker for stable transformation. J. Biol. Chem. *271*, 14010–14019. https://doi.org/10.1074/jbc.271.24.14010.

54. Huynh, M.H., and Carruthers, V.B. (2009). Tagging of endogenous genes in a Toxoplasma gondii strain lacking Ku80. Eukaryot. Cell *8*, 530–539. https://doi.org/10.1128/ec.00358-08.

55. Andenmatten, N., Egarter, S., Jackson, A.J., Jullien, N., Herman, J.P., and Meissner, M. (2013). Conditional genome engineering in Toxoplasma gondii uncovers alternative invasion mechanisms. Nat. Methods *10*, 125–127. https://doi.org/10.1038/nmeth.2301.

56. Meissner, M., Schlüter, D., and Soldati, D. (2002). Role of Toxoplasma gondii myosin A in powering parasite gliding and host cell invasion. Science *298*, 837–840.

57. Pelletier, L., Stern, C.A., Pypaert, M., Sheff, D., Ngô, H.M., Roper, N., He, C.Y., Hu, K., Toomre, D., Coppens, I., et al. (2002). Golgi biogenesis in Toxoplasma gondii. Nature *418*, 548–552. https://doi.org/10.1038/nature00946.

58. Hu, K., Roos, D.S., and Murray, J.M. (2002). A novel polymer of tubulin forms the conoid of Toxoplasma gondii. J Cell Biol. *156*, 1039–1050. https://doi.org/10.1083/jcb.200112086.

59. Pfluger, S.L., Goodson, H.V., Moran, J.M., Ruggiero, C.J., Ye, X., Emmons, K.M., and Hager, K.M. (2005). Receptor for retrograde transport in the apicomplexan parasite Toxoplasma gondii. Eukaryot Cell. *4*, 432–442. https://doi.org/10.1128/EC.4.2.432-442.2005.

60. Hager, K.M., Striepen, B., Tilney, L.G., and Roos, D.S. (1999). The nuclear envelope serves as an intermediary between the ER and Golgi complex in

the intracellular parasite Toxoplasma gondii. J Cell Sci. *112*, 2631–2638. https://doi.org/10.1242/jcs.112.16.2631.

61. Gubbels, M.J., Vaishnava, S., Boot, N., Dubremetz, J.F., and Striepen, B. (2006). A MORN-repeat protein is a dynamic component of the Toxoplasma gondii cell division apparatus. J Cell Sci. *119*, 2236–2245. https://doi.org/10.1242/jcs.02949.

62. Curt-Varesano, A., Braun, L., Ranquet, C., Hakimi, M.A., and Bougdour, A. (2016). The aspartyl protease TgASP5 mediates the export of the Toxoplasma GRA16 and GRA24 effectors into host cells. Cell Microbiol. *18*, 151–167. https://doi.org/10.1111/cmi.12498.

63. Huynh, M.H., and Carruthers, V.B. (2009). Tagging of endogenous genes in a Toxoplasma gondii strain lacking Ku80. Eukaryot Cell. *8*, 530–539. https://doi.org/10.1128/EC.00358-08.

64. Jacot, D., Daher, W., and Soldati-Favre, D. (2013). Toxoplasma gondii myosin F, an essential motor for centrosomes positioning and apicoplast inheritance. EMBO J. *32*, 1702–1716. https://doi.org/10.1038/emboj.2013.113.

65. Li, W., Grech, J., Stortz, J.F., Gow, M., Periz, J., Meissner, M., and Jimenez-Ruiz, E. (2022). A splitCas9 phenotypic screen in Toxoplasma gondii identifies proteins involved in host cell egress and invasion. Nat. Microbiol. *7*, 882–895. https://doi.org/10.1038/s41564-022-01114-y.

66. Eddy, S.R. (2011). Accelerated Profile HMM Searches. PLoS Comput. Biol. *7*, e1002195. https://doi.org/10.1371/journal.pcbi.1002195.

67. Altschul, S.F., Madden, T.L., Schäffer, A.A., Zhang, J., Zhang, Z., Miller, W., and Lipman, D.J. (1997). Gapped BLAST and PSI-BLAST: a new generation of protein database search programs. Nucleic Acids Res. *25*, 3389–3402. https://doi.org/10.1093/nar/25.17.3389.

68. Katoh, K., and Standley, D.M. (2013). MAFFT multiple sequence alignment software version 7: improvements in performance and usability. Mol. Biol. Evol. *30*, 772–780. https://doi.org/10.1093/molbev/mst010.

69. Nguyen, L.T., Schmidt, H.A., von Haeseler, A., and Minh, B.Q. (2015). IQ-TREE: a fast and effective stochastic algorithm for estimating maximum-likelihood phylogenies. Mol. Biol. Evol. *32*, 268–274. https://doi.org/10.1093/molbev/msu300.

70. Stamatakis, A. (2014). RAxML version 8: a tool for phylogenetic analysis and post-analysis of large phylogenies. Bioinformatics *30*, 1312–1313. https://doi.org/10.1093/bioinformatics/btu033.

71. Ronquist, F., Teslenko, M., van der Mark, P., Ayres, D.L., Darling, A., Höhna, S., Larget, B., Liu, L., Suchard, M.A., and Huelsenbeck, J.P. (2012). MrBayes 3.2: efficient Bayesian phylogenetic inference and model choice across a large model space. Syst. Biol. *61*, 539–542. https://doi.org/10.1093/sysbio/sys029.

72. Baek, M., DiMaio, F., Anishchenko, I., Dauparas, J., Ovchinnikov, S., Lee, G.R., Wang, J., Cong, Q., Kinch, L.N., Schaeffer, R.D., et al. (2021). Accurate prediction of protein structures and interactions using a three-track neural network. Science *373*, 871–876. https://doi.org/10.1126/science.abj8754.

73. Remmert, M., Biegert, A., Hauser, A., and Söding, J. (2011). HHblits: lightning-fast iterative protein sequence searching by HMM-HMM alignment. Nat. Methods *9*, 173–175. https://doi.org/10.1038/nmeth.1818.

74. Pettersen, E.F., Goddard, T.D., Huang, C.C., Meng, E.C., Couch, G.S., Croll, T.I., Morris, J.H., and Ferrin, T.E. (2021). UCSF ChimeraX: Structure visualization for researchers, educators, and developers. Protein Sci. *30*, 70–82. https://doi.org/10.1002/pro.3943.

75. Punta, M., Coggill, P.C., Eberhardt, R.Y., Mistry, J., Tate, J., Boursnell, C., Pang, N., Forslund, K., Ceric, G., Clements, J., et al. (2012). The Pfam protein families database. Nucleic Acids Res. *40*, D290–D301. https://doi.org/10.1093/nar/gkr1065.

76. Pattengale, N.D., Alipour, M., Bininda-Emonds, O.R.P., Moret, B.M.E., and Stamatakis, A. (2010). How many bootstrap replicates are necessary? J. Comput. Biol. *17*, 337–354. https://doi.org/10.1089/cmb.2009.0179.

77. Spielman, S.J., and Wilke, C.O. (2015). Pyvolve: A Flexible Python Module for Simulating Sequences along Phylogenies. PLoS One *10*, e0139047. https://doi.org/10.1371/journal.pone.0139047.

78. Zimmermann, L., Stephens, A., Nam, S.Z., Rau, D., Kübler, J., Lozajic, M., Gabler, F., Söding, J., Lupas, A.N., and Alva, V. (2018). A Completely Re-implemented MPI Bioinformatics Toolkit with a New HHpred Server at its Core. J. Mol. Biol. *430*, 2237–2243. https://doi.org/10.1016/j.jmb.2017.12.007.

79. Varadi, M., Anyango, S., Deshpande, M., Nair, S., Natassia, C., Yordanova, G., Yuan, D., Stroe, O., Wood, G., Laydon, A., et al. (2022). AlphaFold Protein Structure Database: massively expanding the structural coverage of protein-sequence space with high-accuracy models. Nucleic Acids Res. *50*, D439-d444. https://doi.org/10.1093/nar/gkab1061.

80. Jumper, J., Evans, R., Pritzel, A., Green, T., Figurnov, M., Ronneberger, O., Tunyasuvunakool, K., Bates, R., Žídek, A., Potapenko, A., et al. (2021). Highly accurate protein structure prediction with AlphaFold. Nature *596*, 583–589. https://doi.org/10.1038/s41586-021-03819-2.

81. Barylyuk, K., Koreny, L., Ke, H., Butterworth, S., Crook, O.M., Lassadi, I., Gupta, V., Tromer, E., Mourier, T., Stevens, T.J., et al. (2020). A Comprehensive Subcellular Atlas of the Toxoplasma Proteome via hyperLOPIT Provides Spatial Context for Protein Functions. Cell host & microbe *28*, 752–766.e9. https://doi.org/10.1016/j.chom.2020.09.011.

82. Team, R.C. (2020). R: A Language and Environment for Statistical Computing (R Foundation for Statistical Computing). https://www.R-project.org/.

83. Stortz, J.F., Del Rosario, M., Singer, M., Wilkes, J.M., Meissner, M., and Das, S. (2019). Formin-2 drives polymerisation of actin filaments enabling segregation of apicoplasts and cytokinesis in Plasmodium falciparum. Elife *8*, e49030. https://doi.org/10.7554/eLife.49030.

84. Schindelin, J., Arganda-Carreras, I., Frise, E., Kaynig, V., Longair, M., Pietzsch, T., Preibisch, S., Rueden, C., Saalfeld, S., Schmid, B., et al. (2012). Fiji: an open-source platform for biological-image analysis. Nat. Methods *9*, 676–682. https://doi.org/10.1038/nmeth.2019.

STAR★METHODS

KEY RESOURCES TABLE

REAGENT or RESOURCE	SOURCE	IDENTIFIER
Antibodies		
c-myc tag	Sigma, cat # M-4439	RRID: AB_439694
HA tag	Roche, cat # 11867431001	RRID: AB_390919
Aldolase	David Sibley	N/A
AMA1	Gift from Gary Ward	N/A
ATPase	Gift from Peter Bradley	N/A
CPN60	Gift from Lilach Sheiner/Swati Agrawal	N/A
Catalase	Markus Meissner	N/A
DrpB	Gift from Peter Bradley	N/A
GAP45	Gift from Dominique Soldati	N/A
ISP1	Gift from Peter Bradley	N/A
M2AP	Gift from Vern Carruthers	N/A
Pro-M2AP	Gift from Vern Carruthers	N/A
MIC3	Markus Meissner	N/A
MIC4	Gift from Dominique Soldati	N/A
ROP1	Gift from J.F. Dubremetz	N/A
ROP2,3,4	Markus Meissner	N/A
ROP5	Gift from Maryse Lebrun	N/A
Anti-mouse Alexa Fluor 488	Invitrogen	RRID: AB_2633275
Anti-rat Alexa Fluor 488	Invitrogen	RRID: AB_2534074
Anti-rabbit Alexa Fluor 488	Invitrogen	RRID: AB_143165
Anti-mouse Alexa Fluor 594	Invitrogen	RRID: AB_2534091
Anti-rat Alexa Fluor 594	Invitrogen	RRID: AB_10561522
Anti-rabbit Alexa Fluor 594	Invitrogen	RRID: AB_2534079
Anti-mouse Alexa Fluor 647	Invitrogen	RRID: AB_162542
Anti-rat Alexa Fluor 647	Invitrogen	RRID: AB_141778
Anti-rabbit Alexa Fluor 647	Invitrogen	RRID: AB_2536183
Anti-mouse Abberior STAR 580	Abberior	Cat# ST580-1001-500UG
Anti-rabbit Abberior STAR 580	Abberior	Cat# ST580-1002-500UG
Anti-mouse Abberior STAR RED	Abberior	Cat# STRED-1001-500UG
Anti-rabbit Abberior STAR RED	Abberior	Cat# STRED-1002-500UG
Anti-mouse IRDye680	Li-Cor	RRID: AB_10956588
Anti-rabbit IRDye680	Li-Cor	RRID: AB_10706167
Anti-mouse IRDye800	Li-Cor	RRID: AB_621847
Anti-rabbit IRDye800	Li-Cor	RRID: AB_621848
Bacterial and virus strains		
DH5alpha *E.coli*	ThermoFisher Scientific	Cat# 18265017
Chemicals, peptides, and recombinant proteins		
Gentamicin	Sigma	Cat# G1397
L-Glutamine	Sigma	Cat# G7513
Fetal bovine serum	BioSell	Cat# FBS.US.0500
Q5 high-fidelity DNA polymerase	NEB	Cat# M0491
Taq DNA polymerase	NEB	Cat# M0267
Mycophenolic acid	Sigma	Cat# M3536

(Continued on next page)

Continued

REAGENT or RESOURCE	SOURCE	IDENTIFIER
Xanthine	Sigma	Cat# X3627
Anhydrotetracyclin (ATc)	Sigma	N/A
Paraformaldehyde	Electron Microscopy Sciences	Cat# 15710
Glutaraldehyde	Sigma	Cat# G7651
Phosphate-buffered saline (PBS)	Sigma	Cat# D8537
Bovine serum albumin (BSA)	Sigma	Cat# A7030
Triton X-100	Roth	Cat# 3051.3
Tween 20	Sigma	Cat# P9416
Prolong Gold Antifade with DAPI	Fisher Scientific	Cat# 11549306
HEPES	Sigma	Cat# H0887
EDTA	Sigma	Cat# EDS-100G
Nonidet P-40 (Tergitol)	Sigma	Cat# NP405
Tris-HCl	Sigma	Cat# T5941
NaCl	Sigma	Cat# S7653
Glycerol	Roth	Cat# 6962.1
Glycine	Roth	Cat# 0079.3
SDS	Roth	Cat# 0183.3
Orange G	Sigma	Cat# O3756-25G
Methanol	Roth	Cat# 0082.2
Calcium ionophore A23187	Merck	Cat# C7522
10x NuPage™ Sample Reducing Agent	Invitrogen	Cat# NP0004
Oligonucleotides		
A list of oligonucleotides can be found in Data S5		
Experimental models: Cell lines		
HFF	ATCC	SCRC-1041™
Experimental models: Organisms/strains		
Toxoplasma gondii RHΔ*hxgpr*t strain	Roos Lab	Donald et al.[53]
T. gondii RHΔKu80	Carruthers Lab	Huynh et al.[54]
T. gondii RHΔKu80DiCre	Meissner Lab	Andenmatten et al.[55]
T. gondii RHΔKu80-TATi	Meissner Lab	Meissner et al.[56]
T. gondii RHΔKu80 ArlX1-3xHA	This work	N/A
T. gondii RHΔKu80 ArlX2-3xHA	This work	N/A
T. gondii RHΔKu80 ArlX3-3xHA	This work	N/A
T. gondii RHΔ*hxgpr*t ArlX2-KO	This work	N/A
T. gondii RHΔKu80 ArlX1-3xHA-KO	This work	N/A
T. gondii TetO7-myc-pSag1-ArlX3 (ArlX3-iKD)	This work	N/A
T. gondii ArlX3-iKD SORTLR-YFP	This work	N/A
Recombinant DNA		
GRASP-RFP	Kristin Hager	Pelletier et al.[57]
ptubmCherryFP-TgTubA1-CAT	John Murray	Hu et al.[58]
GalNacYFP	Manami Nishi	(Unpublished)
TgERD-GFP	Kristin Hager	Pfluger et al.[59]
P30-GFP-HDEL/sagCAT	Boris Striepen	Hager et al.[60]
pmorn1cherryMORN1/sagCAT	Marc-Jan Gubbels	Gubbels et al.[61]
Tub-Cas9-YFP-pU6-ccdB-tracrRNA	Hakimi	Curt-Varesano et al.[62]
LIC 3xHA HX	Meissner	Huynh et al.[63]
pT8TATi1-HX-tetO751myc	Dominique Soldati	Jacot et al.[64]
LIC ArlX1 C-ter-3xHA (pG514)	This work	N/A
LIC ArlX2 C-ter-3xHA (pG514)	This work	N/A

(Continued on next page)

Continued

REAGENT or RESOURCE	SOURCE	IDENTIFIER
LIC ArlX3 C-ter-3xHA (pG514)	This work	N/A
ArlX3 5'UTR gRNA (pG474)	This work	N/A
ArlX1 1st exon gRNA in (pG474)	This work	N/A
ArlX1 disruption gRNA	This work	N/A
ArlX2 disruption gRNA	This work	N/A
ArlX2 disruption gRNA	This work	N/A
puC19YFPFLAG	Meissner	Li et al.[65]
Software and algorithms		
HMMer v3.1b1	Eddy et al.[66]	N/A
BLASTp v2.8.1	Altschul et al.[67]	N/A
MAFFT v7.407	Katoh et al.[68]	N/A
IQ-TREE v1.6.11	Nguyen et al.[69]	N/A
RAxML v8.2.12	Stamatakis et al.[70]	N/A
MrBayes v3.2.7a	Ronquist et al.[71]	N/A
RoseTTAFold https://robetta.bakerlab.org/	Baek et al.[72]	N/A
HHblits (MPI Bioinformatics Toolkit webserver)	Remmert et al.[73]	N/A
ChimeraX	Pettersen et al.[74]	N/A
ImageJ Fiji 1.52f http://imagej.nih.govij	Wayne Rasband NIH	N/A
Image Studio 5.0	Li-Cor	N/A
Zeiss Black software	Zeiss	N/A
LasX software	Leica	N/A
R v3.6.1 and v4.2.1	Team 2020	N/A
RStudio desktop 2022.07.2 + 576	PBC	N/A
Other		
Dulbecco's modified Eagle's medium (DMEM)	Sigma	Cat# D6546
DNeasy Blood and Tissue Kit	Qiagen	Cat# 69504
Extractme genomic DNA kit	Blirt	Cat# EM13
QIAprep Spin Miniprep kit	Qiagen	Cat# 27104
Extractme Plasmid Mini kit	Blirt	Cat# EMO1.1
PCR purification kit	Blirt	Cat# EM26.1
P3 primary cells kit	Lonza	Cat# V4XP-3024
12% Mini-Protean TGX precast polyacrylamide gels	BioRad	Cat# 4561043
Mini-Protean Tetra Vertical Electrophoresis tank	BioRad	Cat# 1658005EDU
Mini-Protean Mini Trans-Blot Module	BioRad	Cat# 1703935
Leica DiM8 widefield microscope	Leica	N/A
Elyra PS.1 SIM microscope	Zeiss	N/A
3D-STED microscope	Abberior	N/A
Jeol 1200 transmission electron microscope	JEOL	N/A
EM 912 transmission electron microscope	Zeiss	N/A
Reichert Ultracut-E ultramicrotome	Leica	N/A
AMAXA 4DNucleofector ™	Lonza	Cat# AAF-1003X
BD FACSAriaIlu Cell Sorter	BD Bioscience	N/A
Odyssey DLx	Li-Cor	N/A

RESOURCE AVAILABILITY

Lead contact

Further information and requests for resources and reagents should be directed to and will be fulfilled by the lead contact, Markus Meissner (markus.meissner@para.vetmed.uni-muenchen.de).

Materials availability

The data underlying this article are available in the article and in its online supplementary material. Cell lines and vectors employed in this article will be shared on reasonable request to the corresponding authors: Joel Dacks (dacks@ualberta.ca) and Markus Meissner (markus.meissner@para.vetmed.uni-muenchen.de).

Data and code availability

- All data reported in this paper will be shared by the lead contact upon request
- Code for the scrollsaw implementation has been deposited in the GitHub repository: https://github.com/chris-klinger/scrollpy.
- Any additional information required to reanalyze the data reported in this work paper is available from the lead contact upon request.

METHOD DETAILS

Homology searching and phylogenetic analysis

Predicted proteomes of all organisms under study were downloaded from relevant public databases; information regarding all datasets is found in Data S4. Initial identification of homologs was performed using HMMer v3.1b1[66] followed by reciprocal BLASTp (v2.8.1)[67] searches against the *Homo sapiens* predicted proteome to check for false positives. All homology searching employed an e-value cut off of 0.05; discrimination between positive and negative hits in reciprocal BLAST used a two order of magnitude cut off, whereby true homologs were considered to hit a relevant homolog in *H. sapiens* with an e-value at least two orders of magnitude greater than the first non-homologous hit. In some cases, additional homologs were identified by reciprocal BLASTp analysis using an identified homolog from the most closely related taxon within the dataset. Domain prediction used PfamScan v1.6[75] with an e-value cut off of 0.01; reported start and stop positions represent the domain "envelope". All results of homology searching and domain prediction analysis can be found in Data S2.

All alignments were carried out using MAFFT v7.407[68]; for alignments less than ~250 sequences, the slow and accurate L-INS-i method was used, while larger alignments used the –-auto option. Alignments were manually inspected and trimmed by hand. IQ-TREE v1.6.11[69] was used for rapid inference of large datasets, under the best model as inferred by each program run and performing 1000 replicates for ultra-fast bootstrapping. RAxML v8.2.12[70] was used both for initial phylogenies during sequence classification, employing maximum-likelihood tree inference and rapid bootstrapping with 100 replicates for each run, and for final bootstrapping of datasets, using the autoMRE criterion to determine a sufficient number of bootstrap replicates for each dataset.[76] In all cases, model selection was performed by RAxML during each program run. Bayesian phylogenies were performed using MrBayes v3.2.7a.[71] Four independent runs of four chains were run for 1,000,000 MCMC generations, sampling every 500 generations under a mixed amino acid model. The consensus tree and statistics were calculated following removal of the first 20% of samples from each run as burn-in. For all phylogenetic inference, rate variation among sites was modeled using a discrete gamma distribution with four rate categories. All trees were viewed using FigTree v1.4.4 (https://github.com/rambaut/figtree) and tree figures manually modified using Affinity Designer v1.6.1 for Mac.

Further sequence filtering used the scrollsaw method of choosing the N best representative sequences from each group among several groups using mutual minimal genetic distance as a selection metric.[5] For simplicity, we wrote a scrollsaw implementation in the Python 3 programming language, available at https://github.com/chris-klinger/scrollpy. Our implementation first aligns sequences before calling the -f x option in RAxML (v8.2.12, run locally with the LG+Γ substitution model)[70] to calculate pairwise maximum-likelihood distances. The program ranks all sequences by mutual minimal ML distance and optionally returns the top N sequences.

To validate this implementation, we ran simulations to generate sequences according to various branch lengths. For each set of branch lengths we generated a random tree with five clades of either three, four, or five sequences each, and then evolved a representative sequence (H. sapiens KLHL8; NP_065854.3) from the root to the tips using Pyvolve v1.0.3[77] (using the LG+Γ with four rate categories and an alpha of 0.5). We calculated all-vs-all distances using the tree branch lengths and between the simulated sequences using our scrollpy implementation; mismatches between the order of each were compared to the total possible number of mismatches given the number of sequences per clade. Running 100 simulations for each yielded an accuracy of 96.67 ± 3.78%, 95.64 ± 3.22%, and 95.58 ± 2.21% for three, four, and five sequences per clade, respectively (Data S6). The small differences between tree and sequence distances may be due to stochasticity in the simulation results; regardless, the simulation results demonstrate that our method accurately selects sequences with mutual minimal distances.

Protein structural prediction

De novo structural prediction used RoseTTAFold[72] hosted at https://robetta.bakerlab.org/. Starting sequences were searched against the Uniref. 30 (2022) database using HHblits[73] as hosted on the MPI Bioinformatics Toolkit webserver[78] with default parameters. The full a3m alignment from HHblits was used together with the starting sequence as inputs to RoseTTAFold. Human structures for comparison were retrieved directly from the AlphaFold protein structure database.[79,80] All protein structures were visualized using ChimeraX[74] and colored using the default "rainbow" coloration.

Analysis of gene co-expression

RNA-Seq gene expression datasets were collected from ToxoDB as previously described.[81] Pearson correlation coefficients between genes were calculated from the FPKM values in R[82] and plotted using the gplots package (v3.1.1).

Parasite and host cell culture

Human foreskin fibroblast (HFF; ATCC designation SCRC-1041) cells were grown in Dulbecco's modified Eagle's medium (DMEM; Sigma, D6546) supplemented with 10% fetal bovine serum (FBS; BioSell FBS.US.0500), 2 mM L-glutamine (Sigma, G7513), and 25 mg/mL gentamicin (Sigma G1397). *T. gondii* strain RH parasites were cultured on confluent HFF monolayers in the same supplemented media. All cells were maintained at 37°C and 5% CO2.

Genomic DNA isolation, cloning, and PCR

To isolate genomic DNA from parasites, roughly 1×10^6 fully egressed parasites were collected and then gDNA was isolated using Qiagen DNeasy Blood and Tissue Kit (Cat. No. 69504) or Extractme genomic DNA kit (Blirt, EM13), as per the manufacturer's instructions. Amplification of DNA segments for cloning used Q5 high-fidelity DNA polymerase (NEB) whereas diagnostic PCR used standard *Taq* DNA polymerase (NEB).

All restriction enzymes for cloning were from NEB, using the high-fidelity (HF) versions, when available. Plasmid preps were made using Qiagen QIAprep Spin Miniprep Kit or Extractme Plasmid Mini Kit (Blirt, EMO1.1), as per the manufacturer's instructions.

We generated tagged lines for each Arl LSP using ligation-independent cloning (LIC), the scheme of which is shown in Figure S5A.[54] Briefly, a C-terminal fragment of each gene to be tagged was amplified by PCR to contain a unique restriction site not present in the LIC vector backbone (for each gene, primers LIC fwd and LIC rev, Data S5). The LIC vector (pG514, Data S5.2) was digested with PacI and then both backbone and insert were treated with T4 DNA polymerase (NEB) prior to ligation. For the vector, 6μL 10X NEB buffer 2, 3 μL 100 mM DTT, 2.4 μL 100 mM dGTP, 1.5μL T4 DNA polymerase, 0.6μL 100X BSA, and 1.2μg of digested vector prep were mixed on ice and the final volume adjusted to 60 μL. For the PCR insert, 2 μL NEB buffer 2, 1 μL 100 mM DTT, 0.8 μL 100 mM dCTP, 0.5 μL T4 DNA polymerase, 0.2 μL 100X BSA, and 0.2 p.m. PCR product were mixed on ice and the final volume adjusted to 20μL. Each separate prep was then incubated in a thermocycler: 30 min at 22°C, 20 min at 75°C, 4°C hold; reactions were held on ice prior to annealing. To anneal, 1μL of treated vector and 2μL of treated insert were mixed and incubated for 10 min at room temperature before addition of 1μL 25mM EDTA and 5 min additional incubation. Annealed vectors were held on ice and used to transform competent bacteria. Each vector was linearized using the corresponding unique restriction enzyme prior to transfection.

All primers used in this study for cloning and diagnostic PCR confirmation of stably transfected cell lines are provided in Data S5.

CRISPR/CAS9 modification of parasites used a single vector encoding both CAS9-NLS-YFP enzyme and pTgU6-gRNA.[62] To generate vectors containing a specific gRNA, the gRNA was synthesized as complementary primers (for each gene, primers gRNA fwd and rev, Data S5). Primers were suspended in annealing buffer (10mM Tris pH 7.5, 50mM NaCl, and 1mM EDTA), heated to 95°C, and then allowed to cool to room temperature. The parental vector was digested with BsaI and then gRNA inserts were ligated into the digested vector using T4 DNA ligase (NEB).

Repair template for integration of a tag in the *sortlr* locus was generated as previously described.[83] The repair template was purified using a PCR purification kit (Blirt; EM26.1).

Transfection of parasites

Transfections were carried out using an AMAXA 4DNucleofector (Lonza; AAF-1003X) and the P3 primary cells kit (Lonza; V4XP-3024) as previously described.[65] The program FI-158 was used for electroporation. Transient transfections used ~10 μg of purified DNA and ~1×10^5 freshly egressed parasites, whereas stable transfections used ~20–30 μg of purified DNA and ~1×10^6 freshly egressed parasites. DNA for transfection was ethanol precipitated and resuspended in P3 Buffer. In the case of stable transfection, integration was selected for by supplementing culture medium with 78 μM mycophenolic acid (MPA; Sigma; M3536) and 230 μM xanthine (Sigma; X3627)[53]; selected pools were then cloned by limiting dilution in 96 well plates and individual clones picked and analyzed. All vectors used for transfection are listed in Data S5.

This tagging was carried out in parasites lacking ku80 but stably expressing split Cre recombinase (Δku80-diCre); this parental line was chosen in case Cre-mediated gene excision was required (though this option was not explored in this study). For each line, genomic DNA and protein was collected in order to confirm proper integration and expression by both integration PCR and Western blotting (Figure S5B–S5H).

In order to generate Arl LSPs KO via CRISPR/Cas9 mediated disruption, we transiently transfected vectors containing a fusion of Cas9 and YFP, that allows identification of transfected parasites, together with the cassette for the expression of the single guide RNA (sgRNA) targeting the gene of interest (GOI).[39,40] To find an effective guide RNA (gRNA), we selected one already employed in Sidik et al. 2016.[41] The localisation of the targeted sequence and the phenotypic score annotated for that specific sgRNA is displayed in Figure S6E. All sgRNA targeted the main Arf-ADF ribosylation factor domain. After 48 h post transfection, parasites were fixed and labeled with different antibodies targeting secretory organelles such as micronemes (MIC4 and Mic8), rhoptries (ROP1 and ROP2,4), endosomal like compartment (ECL, Pro-M2AP) and Trans-Golgi network (TGN; DrpB).

Generation of ArlX3-iKD was achieved by integration of a PCR fragment containing the p*dhfr-hxgprt*-3′UTR*dhfr*- TetO7-myc-pSag1 cassettes with 50 nucleotides (nt) of homology to the promoter of ArlX3 and 50nt of homology to the n-terminus of ArlX3 in

each side of the amplicon. Parasites were transfected with both donor DNA and a CAS9-YFP vector a gRNA targeting the N terminus of this gene. Parasites were selected with 78μM mycophenolic acid (MPA; Sigma; M3536) and 230μM xanthine (Xan. Sigma; X3627)[53]; selected pools were then cloned by limiting dilution in 96 well plates and individual clones picked and analyzed;

Tagging of SORTLR with the yellow fluorescent protein (YFP) was achieved by simultaneous transfection of a specific CAS9-YFP-gRNA vector with a PCR amplicon as donor containing 50 nt of homology to *sortlr* in each side of the YFP cassette. Parasites expressing Cas9-YFP were sorted via FACS (FACSARIA III, BD Biosciences) into 96-well plates (a minimum of 3 events per well). Resultant clonal parasites were screened by PCR and repair template integration confirmed by sequencing.[65]

Immunofluorescence assays

HFF cell confluent monolayers on glass coverslips were infected with parasites. Parasites were fixed using 4% paraformaldehyde (PFA) at room temperature for 20 min before being washed three times with 1X phosphate-buffered saline (PBS). Subsequently, coverslips were permeabilized and blocked using blocking buffer (3% BSA and 0.2% Triton X-100 in 1X PBS (PBS-TX-100)) for 1 h at room temperature. Primary antibodies were added to blocking buffer at the dilutions indicated in Data S5, and cells stained for 1 h at room temperature before being washed three times with PBS-TX-100. Similarly, secondary antibodies (Life Technologies) were added to blocking buffer and cells stained for 1 h at room temperature in the dark. Samples were washed three more times with PBS-TX-100 and then coverslips were mounted using either mounting media alone or mounting media supplemented with DAPI. Non permeabilizing IFAs were performed as above, but without the addition of TX-100 to blocking and wash buffers.

Plaque assay

For plaque assays, 1×10^3 freshly egressed parasites were added to a confluent HFF monolayer with or without addition of 1 μg/mL ATc. After five days, cultures were washed once with PBS and then fixed with ice-cold methanol for 20 min. Methanol was removed and cells stained with Giemsa, followed by three washes with PBS. All plaques in 10 random fields of view were measured using Fiji for three independent experiments. Raw data are provided in Source data.

Gliding assay

1×10^6 freshly egressed parasites were suspended in pre-warmed gliding buffer (1mM EDTA and 100mM HEPES) and allowed to glide on glass coverslips coated with FBS for 30 min prior to fixation with 3% PFA. An IFA was performed using α-SAG1 primary antibody under non-permeabilising conditions to label deposited trails. One hundred random parasites were assessed for the presence/absence of trails in three independent experiments and the mean and SEM were calculated. Raw data are provided in Source data.

Invasion-replication assay

5×10^4 freshly egressed parasites were allowed to invade confluent HFFs pre-seeded onto coverslips for 1 h before several washes with PBS were performed to remove uninvaded parasites. 24 h later, cells were fixed with 4% PFA and an IFA was done with α-GAP45 primary antibody. For the invasion assays, the number of vacuoles in 15 random 40X fields of view were counted for three independent experiments, and the mean and SEM calculated.

For the replication assays for ArlX3-KD, parasites were pre induced with or without ATc for 48h prior the infection of coverslips pre-seeded with HFFs. Parasites were allowed to invade for an hour and wells were washed 3 times before incubation for 24 h at 37C and 5% CO_2. After fixation, parasites were labeled with α-GAP45 and α-Myc to assess the downregulation of ArlX3 prior quantification of the number of parasites per vacuole. At least 900 random vacuoles from 3 biologically independent experiments were counted. Raw data are provided in Source data.

Egress assay

For egress assays, 5×10^4 freshly egressed parasites were allowed to invade confluent HFFs for an hour. 36 h later, culture media was exchanged for pre-warmed DMEM without FBS with 2 μM calcium ionophore (A23187) to induce egress. Five minutes after media exchange, cells were fixed with 3% PFA and subsequently stained with α-SAG1 antibody under non-permeabilising conditions (together with DAPI to assess intracellular vacuoles). One hundred random vacuoles were assessed for egress ability in three independent experiments, and the mean and SEM calculated. Raw data are provided in Source Data.

Western blotting and protein detection

Approximately 1×10^7 freshly egressed parasites were harvested and pelleted by centrifugation at 5000 rpm followed by a single wash with 1X PBS. The parasite pellet was lysed on ice with NP-40 buffer (50 mM Tris-HCl pH 7.5, 150 mM NaCl, 1% Nonident P-40, and 4mM EDTA) and incubated for 5 min on ice. Insoluble material was pelleted by centrifugation at 14,000 rpm at 4°C. The supernatant was placed in a new tube together with 10X NuPage Sample Reducing Agent (Invitrogen) and 4X loading buffer (125mM Tris-HCl pH 6.5, 50% v/v glycerol, 4% w/v SDS, 0.2% w/v orange G). Samples were boiled for 10 min at 95°C, loaded onto 12% Mini-Protean TGX Precast polyacrylamide gels (BioRad), and run at 130V. Samples were transferred to nitrocellulose using a Mini-Protean transfer tank containing 1L of transfer buffer (48mM Tris, 39mM glycine, and 20% methanol) running at 400mA for 1 h. Membranes were blocked using 5% skim milk powder in 1X PBS at room temperature for 1 h. Primary antibodies were added at the appropriate concentration (Data S5) in blocking buffer (5% skim milk powder in 1X PBS +0.2% Tween 20 (PBS-TW-20) for 1 h. Membranes were washed three

times with PBSTW-20, before addition of IRDye680RD and IRDye800RD secondary antibodies (Li-Cor) in blocking buffer for a further hour. Membranes were washed three times in PBS-TW-20 followed by an additional wash in 1X PBS to remove Tween 20 prior to imaging. Detection of infrared signal was performed using a Li-Cor Odyssey with Image Studio 5.0 software (Li-Cor).

Structured illumination microscopy (SIM)
For SIM imaging we used an ELYRA PS.1 microscope (Zeiss) equipped with a Plan Apochromat 63x, 1.4 NA oil immersion lens and CoolSNAP HQ camera (Photometrics). SIM processing of captured images used ZEN Black software (Zeiss) and all subsequent processing used Fiji ImageJ.[84]

Electron microscopy
Induced and non-induced intracellular parasites were fixed with 2.5% (v/v) glutaraldehyde in 0.1 M phosphate buffer, pH 7.4, after the indicated incubation. The parasites were washed three times at room temperature with PBS (137 mM NaCl2, 2.7 mM KCl, 10 mM Na2HPO4, 1.8 mM KH2PO4, pH 7.4) and postfixed with 1% (w/v) osmium tetroxide for 1 h. Subsequent to washing with PBS and water, the samples were stained *en bloc* with 1% (w/v) uranyl acetate in 20% (v/v) acetone for 30 min. Samples were dehydrated in a series of graded acetone and embedded in Epon 812 resin. Ultrathin sections (thickness: 60 nm) were cut using a diamond knife on a Reichert Ultracut-E ultramicrotome. Sections were mounted on collodium-coated copper grids, post-stained with lead citrate (80 mM, pH 13), and examined with an EM 912 transmission electron microscope (Zeiss, Oberkochen, Germany) equipped with an integrated OMEGA energy filter operated in the zero-loss mode at 80 kV. Images were acquired using a 2k × 2k slow-scan CCD camera (Tröndle Restlichtverstärkersysteme, Moorenweis, Germany).

For cryo-immunolabeling, the samples were fixed in phosphate buffer, pH 7.2, containing 4% freshly prepared formaldehyde. After several washes in the same buffer, they were embedded in 10% gelatin at 37°C for 30 min. The material was spun down and the samples were left on ice for 30 min. After confirming the gelatine was solid, the pellet was removed from the tubes and infiltrated overnight in 2.1 M sucrose and rapidly frozen by immersion in liquid nitrogen. Cryo-sections (70 nm thick) of the frozen material were obtained at −120°C using an Ultracut cryo-ultramicrotome (Leica Microsystems). The cryo-sections were collected on formvar-coated nickel grids, thawed, and put on a cushion of 2% gelatine. The grids were left for 20 min at 37°C and then blocked in PBS containing 3% bovine serum albumin for 1 h. After this time, they were incubated in the presence of primary antibody. Then they were washed several times in blocking buffer and incubated with 15 nm gold-conjugated Protein A (Aurion). The grids were washed several times in the blocking buffer, dried, and contrasted in a mixture of methylcellulose/uranyl acetate. All images were captured on a Jeol 1200 transmission electron microscope (JEOL, Japan) operating at 80kV and analyzed/processed with Fiji software.

Quantitative fluorescence microscopy and image analysis
Time-course quantification of TATi-ArlX3 knockdown protein levels was carried out as follows. Parental Δku80-TATi and TATi-ArlX3 parasite lines were induced for the relevant time periods with 1 μg/mL ATc and processed for IFA using α-myc and α-GAP45 antibodies.

Quantitative fluorescence analysis were performed in images captured using the same excitation parameters on a Leica DiM8 widefield fluorescence microscope equipped with an HC PL APO 100x/1.44 oil immersion lens (Leica) and C13440-20C CMOS camera (Hamamatsu). STED microscopy was performed in the Abberior 3D STED microscope. Images were then analyzed with ImageJ Fiji v1.53q.

Image files were loaded into Fiji and z-stacks collapsed into 2D images by summation of individual slices. For each vacuole, a region of interest (ROI) was traced in Fiji, using the α-Gap45 signal to indicate the bounding region of parasites in each vacuole. These ROIs were subsequently used to measure area, integrated density, and mean gray value in the α-myc channel. For each ROI, similar measurements were also obtained for the local background in the α-myc channel where no vacuoles were present. Subsequently, corrected total cell fluorescence was calculated as integrated density – (vacuole area x mean background fluorescence), as described previously.[42] One hundred random vacuoles were quantified for each of three independent experiments. Raw data are provided in Source data.

For the analysis of Golgi vesiculation with the SORTLR marker, parasites were induced with or without ATc for 24, 48 and 72h, fixed and imaged as described above. Images were processed in Fiji and Z-stacks were collapsed into 2D images by applying maximum projection. A global thresholding was employed to mark vesicles in single vacuoles and particles bigger than 0.01 μm were analyzed to calculate number of vesicles, area and mean intensity. Outlines of thresholding were obtained. At least 10 vacuoles per time-point per replicate (3 biologically independent replicates) were analyzed. Mean and SEM were calculated and plotted. Raw data are provided in the Source data file.

Pearson's correlation (r) was calculated in Fiji using the plugin JACoP.[43] Parasites were induced with or without ATc for 24, 48 and 72h fixed and α-myc antibody was used to visualised ArlX3. A single stack was isolated for the analysis of the correlation. 90 vacuoles from 3 biologically independent replicates in each time-point. Mean and SEM were calculated. Raw data are provided in the Source data file.

QUANTIFICATION AND STATISTICAL ANALYSIS

All statistical analysis was performed in R v3.6.1 and v4.2.1.[82] Comparisons among multiple means used one-way ANOVA followed by post-hoc Tukey's HSD test when assumptions of normality and equal variance were not significantly violated; in cases where violation did occur, Kruskal-Wallis followed by post-hoc Dunn's test was used instead. Comparison between plaque sizes in plaque assay used two-way ANOVA and means within each group were compared by a Wilcoxon signed rank test. Comparison of multiple populations within a single group (e.g., for phenotypic analysis) used Chi-square followed by post-hoc Fisher's exact test. All plots were made in R and the first instance of significant difference from controls indicated.